Improvements to the Reconstruction of Monoscopic Events in H.E.S.S., with Application to the Analysis of a Flare of the Blazar PKS 0903-57

Master's Thesis

submitted to
Indian Institute of Science Education and Research Tirupati
in partial fulfillment of the requirements for the
BS-MS Dual Degree Programme

by

Anita Deka Baruah
Roll Number: 20191096

Supervisor: Prof. Dr. James Anthony Hinton
Max-Planck-Institut für Kernphysik, Heidelberg, Germany

April 1, 2024

Abstract

The High Energy Stereoscopic System is an array of five imaging atmospheric Cherenkov telescopes that detects air showers produced by very high energy γ-rays. To exploit the full energy range of the experiment (tens of GeV upto 100 TeV), a combined analysis of detected γ-ray events of various quality classes needs to be carried out. In particular, the events detected by the 28m telescope (CT5) are very important because they are mostly at low energies and a stereoscopic view aiding the reconstruction of the air shower is not possible. In this thesis, we present improvements carried out on CT5's energy and angular monoscopic reconstruction. We utilise next-generation air shower simulations, new image parameters and machine learning tools such as artificial neural networks for this work. Furthermore, upon implementing these improvements in the H.E.S.S. data analysis chain, we carry out a high-level Gammapy analysis of the 2020 H.E.S.S. observations of the flaring blazar PKS 0903-57.

This work sets the ground for ongoing and future work on finalising the implementation of the various event quality classes in the H.E.S.S. pipeline, which shall ultimately boost the sensitivity of the experiment for the detection of γ-ray bursts and flares from distant active galactic nuclei.

Acknowledgements

First and foremost, thank you to my supervisors Jim Hinton, Laura Olivera-Nieto and Lars Mohrmann for taking me on as as a master’s intern at MPIK, and for their invaluable guidance and encouragement. I am forever grateful to them, the non-thermal astrophysics group and my officemates for making me one of their own. A special thank you to Simon Steinmaßl for his infinite patience and to Rodrigo Guedes Lang and the H.E.S.S. group from whom I got to learn so much.

A huge thanks to Ankush and Prajath, who made the move to Heidelberg so easy and the latter for all the times he allowed me to break his lines of thought over my broken lines of code. To Jacob and Madita for making everything feel like home with their cooking, baking and for the ultimate WG experience. Thank you to Ainesh and Aryan for sharing this journey at IISER Tirupati with me and so much more. To my roommates over the first four years at IISER and the amazing Supriya for her endless support and kindness, both offline and on. To the fellow interns in Germany and France, who concocted and executed the December trip to perfection.

Finally, a gigantic thank you to my parents and (little) brother, without whom none of this would be possible. And to Georg Schwefer – danke schön.

Contents

List of Figures

List of Tables

List of Abbreviations

VHE	**V**ery **H**igh **E**nergy
HE	**H**igh **E**nergy
H.E.S.S.	**H**igh **E**nergy **S**tereoscopic **S**ystem
AGN	**A**ctive **G**alactic **N**uclei
GRB	**G**amma **R**ay **B**urst
Fermi-**LAT**	Fermi-**L**arge **A**rea **T**elescope
EAS	**E**xtensive **A**ir **S**hower(s)
CR	**C**osmic **R**ay
EM	**E**lectro-**M**agnetic
UHE	**U**ltra **H**igh **E**nergy
IACT	**I**maging **A**tmospheric **C**herenkov **T**elescope
PMT	**P**hoto-**M**ultiplier **T**ube
CT(1-5)	**C**herenkov **T**elescope (1-5)
FoV	**F**ield of **V**iew
MC	**M**onte **C**arlo
NSB	**N**ight **S**ky **B**ackground
GHS	**G**amma **H**adron **S**eparation
BDT	**B**oosted **D**ecision **T**ree
PSF	**P**oint **S**pread **F**unction
SMBH	**S**uper**m**assive **B**lack **H**ole
LoS	**L**ine of **S**ight
FSRQ	**F**lat **S**pectrum **R**adio **Q**uasar
SED	**S**pectral **E**nergy **D**istribution
IC	**I**nverse **C**ompton
SSC	**S**ynchrotron **S**elf-**C**ompton
EBL	**E**xtragalactic **B**ackground **L**ight
CMB	**C**osmic **M**icrowave **B**ackground
HAP	**H**.E.S.S. **A**nalysis **P**ipeline
ANN	**A**rtificial **N**eural **N**etwork

ML	**M**achine **L**earning
TMVA	**T**oolkit for **M**ulti**V**ariate Data **A**nalysis
CoG	**C**entre of **G**ravity
FO	**F**ixed **O**ffset
DNN	**D**eep **N**eural **N**etwork
EDI	**E**nergy **D**isp **I**mpact
CM	**C**onfusion **M**atrix
BFF	**B**ad **F**lip **F**raction
NN	**N**eural **N**etwork
TS	**T**est **S**tatistic

Introduction

Very-high-energy (VHE) or TeV-scale γ-rays probe some of the most extreme environments in the Universe such as active galactic nuclei (AGN), pulsar wind nebulae, gamma-ray bursts (GRBs) and supernova remnants. When a VHE γ-ray strikes the earth's atmosphere, it produces a cascade of relativistic charged particles, called an extensive air shower (EAS), which gives off a flash of Cherenkov radiation. Ground-based imaging atmospheric Cherenkov telescopes (IACTs), such as the high energy stereoscopic system (H.E.S.S.), image this Cherenkov radiation.

The H.E.S.S. array of IACTs comprises 5 telescopes — four smaller telescopes with a diameter of 12m (called CT1-4) and a central 28m telescope (called CT5). This arrangement allows the simultaneous observations of an air shower to be carried out. The presence of five telescopes allows a stereoscopic reconstruction of the primary γ-ray's direction of arrival and energy.

Owing to its larger mirror and camera, CT5 is able to detect relatively lower energy events than the other four telescopes, down to a threshold of 10s of GeV. It, therefore, contributes crucially to the sensitivity achieved by the experiment at low energies. However, most low-energy events seen by CT5 are not imaged by the smaller telescopes, thereby making a stereoscopic view impossible. A monoscopic reconstruction of events, therefore, becomes necessary in order to access the full energy range of H.E.S.S..

With limited information available from only one telescope, monoscopic reconstruction is difficult and leads to a loss in accuracy of further scientific analysis carried out on monoscopic data. New techniques to overcome this problem have been proposed — by including more information (through shower image parameters) in the direction reconstruction algorithms and employing machine learning (ML) methods. In this thesis, such improvements to the monoscopic reconstruction in H.E.S.S. are developed, implemented and tested.

Correctly reconstructing the directions and energies of γ-ray events is a crucial step in the study of astrophysical sources. With improved monoscopic reconstruction, the sensitivity of H.E.S.S. at low energies is increased, a critical range for the study of non-thermal processes in a variety of sources, such as AGN and

GRBs. Moreover, in addition to serving as groundwork for improved reconstruction techniques in the future, the improvements carried out to mono reconstruction described in this thesis form part of a larger-scale project of implementing a uniform framework of data analysis for H.E.S.S..

This thesis is organised as follows:

- Chapter 1 introduces the field of very high energy γ-ray astrophysics and the H.E.S.S. experiment, and also provides a brief overview of the data analysis chain employed therein. The chapter concludes with a discussion on AGN, which serve as science targets for this work.
- Chapter 2 offers an overview of the drawbacks of the present analysis chain employed in H.E.S.S. and the alternative ways of addressing these problems. In particular, the task at hand — improving the capabilities of the central largest telescope in H.E.S.S. — is introduced.
- Chapter 3 provides an introduction to artificial neural networks as tools to address the limitations of the current H.E.S.S. pipeline.
- Chapter 4 presents the results of the improvements carried out to the H.E.S.S. analysis chain, with a focus on the simulation-based data.
- Chapter 5 presents the results of carrying out a high-level analysis of the benchmark target (a VHE AGN source observed with H.E.S.S.), with a particular emphasis on the improved analysis configuration. A comparison with the previous analysis, without improvements, is also presented and discussed.
- Chapter 6 summarises the work carried out in this thesis, and presents the ground for future work.

Chapter 1

Very High Energy (VHE) γ-ray Astrophysics

High-energy astrophysics is the study of astrophysical phenomena that involve the emission of high-energy, non-thermal photons (X-rays and γ-rays). In particular, this field involves the study of fundamental physics taking place in highly violent and relativistic scenarios, usually around compact objects such as black holes and neutron stars of different scales [1]. These sources also produce non-electromagnetic signals such as cosmic rays (CRs), gravitational waves and neutrinos which, if studied in conjunction with their γ-ray emission, can offer a holistic picture of the non-thermal universe [2, 3].

Out of the broad-band, non-thermal electromagnetic radiation spectrum from these objects, the γ-ray emission itself extends several orders of magnitude in energy, reaching ranges beyond the scope of terrestrial particle accelerators. The lower end of energies spanned by γ-rays is termed the *high energy (HE)* regime, with photon energies lying in the range 100 MeV-100 GeV. *Very high energy (VHE)* γ-rays have energies exceeding 100 GeV and upto a 100 TeV.

In this chapter, an overview of the processes and techniques involved in the detection of VHE γ-rays on the ground is presented. This is accompanied by an introduction to the High Energy Stereoscopic System (H.E.S.S.), the instrument of focus in this work, and a review of the γ-ray data analysis pipeline employed therein. Finally, a a specific type of VHE γ-rays source, namely active galactic nuclei (AGN), that are employed as benchmark and validation cases in this work is discussed.

1.1 Ground-based γ-ray astronomy

Earth's atmosphere is opaque to radiation beyond optical wavelengths and entirely blocks out X-ray and γ-ray radiation from cosmic sources. Therefore, the direct detection of γ-rays is only possible with space- and balloon-borne experiments; the Fermi-Large Area Telescope (LAT), for instance, has been highly instrumental in several outstanding discoveries of γ-ray sources [4].

However, when photon energies reach tens of GeV, a two-fold problem for such detectors arises. Firstly, the spectrum followed by γ-rays arriving at Earth is a *power-law*, $\frac{dN}{dE} \propto E^{-\Gamma}$ (Γ is the *spectral index*) – the flux of photons decreases rapidly with increasing energy. Thus, for good statistics at high γ-ray energies, large collecting areas and long exposure times are needed, which are massive practical and technological challenges [5]. Secondly, it becomes exceedingly difficult to find material that can "stop" such VHE γ-rays for detection [3]. Space-based detectors are, therefore, appropriate for the detection of γ-rays with energies only in the HE regime.

At very high energies, a unique opportunity to carry out γ-ray astronomy from the ground arises. Although astrophysical γ-rays can not penetrate the atmosphere to reach Earth's surface, they do interact with nuclei in the atmosphere to produce air showers of secondary particles, which can be detected by a variety of techniques on the ground. The atmosphere can, thus, be employed as a gigantic gas detector to study VHE cosmic γ radiation [2, 3, 6, 7].

1.1.1 Extensive air showers (EAS)

A high-energy particle (γ-ray photon or electron or CR) can interact with atmospheric nuclei through a variety of processes and give rise to a cascade of relativistic secondary particles and photons, termed an "*extensive air shower*" (EAS). Depending on the initial particle, the interactions may be primarily hadronic or electromagentic, which leads to an intrinsic variability in shower production. Since an overwhelming fraction of such showers are initiated by CRs, understanding the subtle variations in the detectable products of an EAS is required to discriminate signal (γ-rays) from background (CRs) [5, 6].

The EAS produced by a VHE γ-ray is governed mainly by two physical processes: *pair production* and *Bremsstrahlung*. A primary γ-ray interacts with the Coulomb field of an atmospheric nucleus and produces an electron-positron ($e^{\pm}$) pair. These, in turn, loose energy by Bremsstrahlung to further produce γ-rays. With successive pair production and Bremsstrahlung, an electromagnetic cascade develops (Figure 1.1a). This is termed an *electromagnetic (EM) shower*. The growth of the shower stops

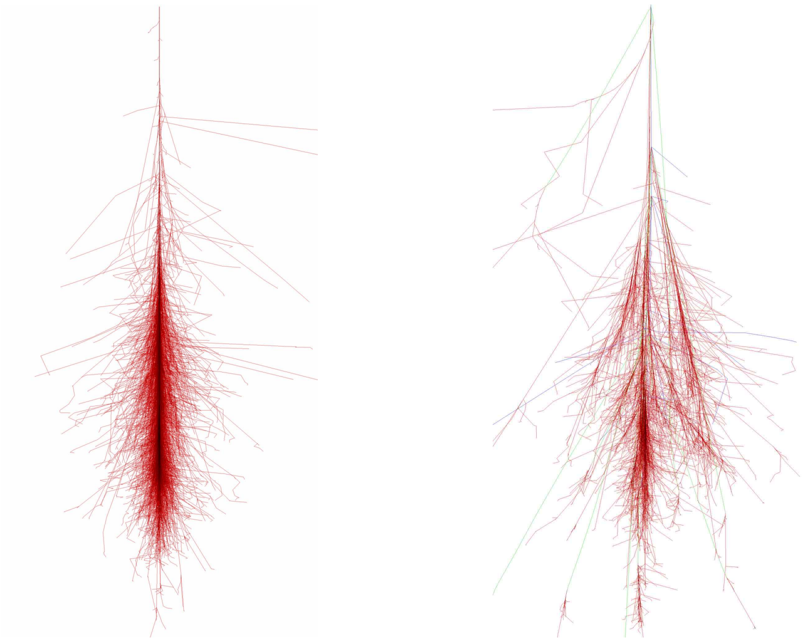

(A) EM shower (B) Hadronic shower

FIGURE 1.1: Lateral profiles of simulated EAS produced by (A) a γ-ray and (B) a cosmic ray proton, each with an energy of 100 GeV. Images courtesy of the CORSIKA site; CORSIKA (COsmic Ray SImulations for KAscade) is a program used for the production of highly-detailed air shower simulations [8].

when the energies of the constituent particles reach a critical energy, below which ionization losses dominate [9].

On the other hand, the EAS produced by a hadron colliding with atmospheric nuclei (termed *hadronic showers*) are more complicated to describe and unlike an EM shower, comprise of several components (Figure 1.1b). The hadronic component of the shower consists of pions ($\pi^{0,\pm}$) and kaons ($K^{\pm}$) as well as spallation products such as nuclear fragments. Neutral pions (π^0) decay into γ-rays, which can form an electromagnetic shower component in much the same way as described before. Charged mesons ($\pi^{\pm}$ and $K^{\pm}$) decay into high energy muons ($\mu^{\pm}$) and atmospheric neutrinos forming the leptonic component. In this case, shower development stops when pion energies go below a critical energy [6, 9].

Ground-based γ-ray astronomy relies on the detection of γ-ray EAS by employing either of the following two techniques:

- **Atmospheric Cherenkov technique**: Ultra-relativistic particles in an EAS travel faster than the speed of light in air and emit Cherenkov radiation (see following Section 1.1.2). The time-scale of this Cherenkov light wavefront is in nanoseconds. Detectors using this technique sample this Cherenkov light from complete showers (EAS that have died out before reaching the ground).

In this case, the atmosphere acts as a giant calorimeter – the total amount of Cherenkov light is proportional to the energy of the primary particle [6]. Although these detectora have very short duty cycles (around 15%), they provide superior background rejection and angular resolution [5, 2, 7].

- **Particle sampler technique**: Detectors utilizing this technique measure the shower tail reaching the ground. Experiments employ arrays of water or scintillator detectors to detect the charged secondaries and are called *air shower arrays*. They also provide a unique window into the ultra-high energy (UHE) regime (energies > 100 TeV) because they have large fields of view and very long duty cycles (almost 100%). This also makes them ideal for sky surveys and detecting transient sources [5].

1.1.2 Cherenkov radiation

Cherenkov light is produced when charged particles travel through a dielectric material with velocities greater than the speed of light in that medium. For a particle moving with a velocity v_p through a medium with refractive index $n = \frac{c}{v}$ (here v is the speed of light in that medium), a dipole field symmetric along the azimuth is produced (Figure 1.2) [10].

When the particle travels at relativistic speeds, $v_p > v = \frac{c}{n}$, a coherent depolarization of the dielectric medium leads to the emission of a cone of Cherenkov light. This cone has an opening angle θ_c such that

$$cos(\theta_c) = \frac{c}{nv_p} = \frac{1}{n\beta}, \tag{1.1}$$

where $\beta = \frac{v_p}{c}$.

The minimum energy, E_{min}, required by a particle of mass m_0 with Lorentz factor γ_{min}, to produce Cherenkov radiation is

$$E_{min} = \gamma_{min} m_0 c^2 = \frac{m_0 c^2}{\sqrt{1 - n^{-2}}} \tag{1.2}$$

where $\gamma_{min} = 1/\sqrt{1 - {v_p}^2/c^2}$ and $v_p = v$ at the threshold. Therefore, particles with smaller masses (small m_0) such as electrons and positrons tend to dominate the Cherenkov light pool; for instance, in air, their energy threshold is ~21 MeV as compared to ~4.4GeV for muons.

The *Cherenkov yield*, that is the number of photons emitted per unit track length of the charged particle, dz, and per unit wavelength, $d\lambda$, is given by the *Frank-Tramm*

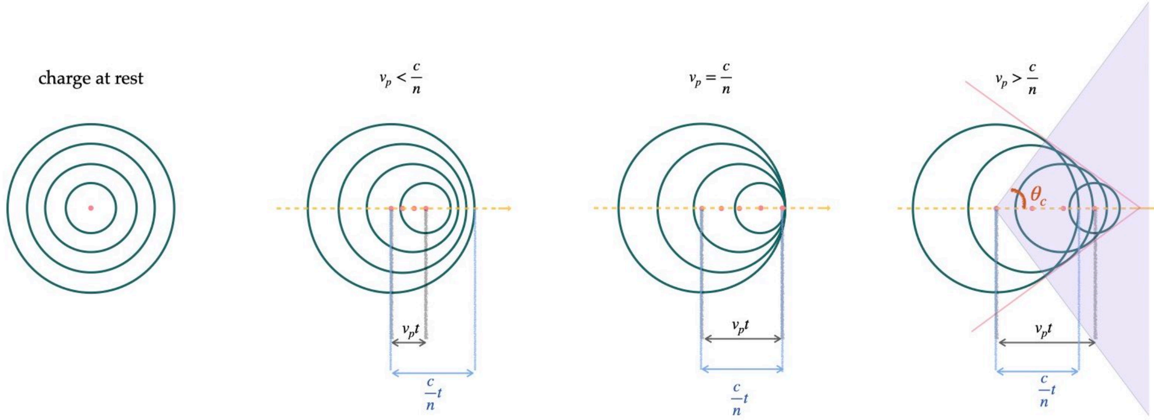

FIGURE 1.2: Cherenkov light emission from a particle moving at relativistic speeds (velocity greater than the speed of light in the medium). The radiation is emitted in a cone with opening angle θ_c (extreme right). The figure is adapted from [10] and [11].

equation [10, 6]:

$$\frac{\mathrm{d}^2 N_{ph}}{\mathrm{d}z\mathrm{d}\lambda} = 2\pi\alpha Z^2 \frac{sin^2\theta_c}{\lambda^2} = 2\pi\alpha Z^2 \frac{(1-(\beta n(\lambda))^{-2})}{\lambda^2}. \tag{1.3}$$

Here, $\alpha \approx 1/137$ is the fine-structure constant and Z is the charge of the particle. Note the $1/\lambda^2$ dependence – Cherenkov light peaks at shorter wavelengths corresponding to the UV-blue region.

1.2 Imaging Atmospheric Cherenkov Telescopes (IACTs)

Imaging Atmospheric Cherenkov Telescopes (IACTs) employ the Atmospheric Cherenkov technique (Section 1.1.2) to image the ns-long flashes of Cherenkov radiation produced by an EAS. Since the Cherenkov photons are spread across a large circular area, one or multiple telescopes placed in this light pool can detect such a shower and provide collecting areas of the order of km^2 [6, 7, 12].

IACTs comprise of an optical reflector, which focuses the faint, blue Cherenkov light onto a camera consisting of several *photomultiplier tubes* (PMTs). Along with very fast front-end electronics, PMTs provide the acutely sensitive and ultra-fast response needed to image the ns-long flashes. Thus, an EAS, which can either be a γ-ray or CR-initiated one, triggers one or more telescopes through its Cherenkov light and a resultant image, termed an "event", is obtained by each telescope.

Each event contains information about the primary γ-ray's energy and direction. An array of IACTs, such as H.E.S.S., can provide a stereoscopic view of an EAS, therefore allowing for a much more accurate reconstruction of the shower (and thus the primary γ-ray) direction. Note that due to the very low intensity of the blue Cherenkov light, these telescopes can only operate during the night and their functioning is severely affected by moonlight and atmospheric conditions.

1.2.1 The H.E.S.S. array

Located in the Khomas Highlands of Namibia in Southern Africa, the *High Energy Stereoscopic System* (H.E.S.S.) is an array of five IACTs. It is sensitive to γ-rays with energies ranging from tens of GeV to a tens of TeV [13].

FIGURE 1.3: A full view of the H.E.S.S. array with the four small (CT1-4) telescopes and central large telescope (CT5). Picture credit: the H.E.S.S. Collaboration [14].

Four of the five telescopes, referred to as *CT1-4* (CT for Cherenkov Telescope), are arranged in the form of a square with side length 120 m and were contructed as part of the first phase of the experiment (called H.E.S.S. I). Each of these four telescopes is equipped with a segmented mirror of 12 m diameter which is mounted on an alt-azimuth setup. The camera of each telescope comprises 960 PMTs (pixels) which collect the Cherenkov radiation from an EAS and has a 5° field of view (FoV). The CT1-4 telescopes offer a stereoscopic view of the same air shower [13].

The fifth telescope, with a 28 m parabolic mirror that corresponds to a collecting area of 650 m^2, is the largest of the five. It is placed in the center of the array (See

Figure 1.3). Called *CT5*, this telescope has a much larger camera with 2048 PMTs and has a FoV of 3.5°. CT5 significantly increases the sensitivity and energy coverage of the instrument at low energies due to its greater size and sensitive camera. The five telescopes now make up the second phase of the experiment (H.E.S.S. II) [13, 15, 16].

1.3 Data analysis in IACTs

The raw data from IACTs – images of EAS seen through their Cherenkov light – undergo several steps of processing in order to obtain workable science products. Figure 1.4 shows an overview of the various stages in this analysis chain, which are briefly described in this section, along with the very important role played by Monte Carlo simulations of EAS (such as the CORSIKA simulations in Figure 1.1).

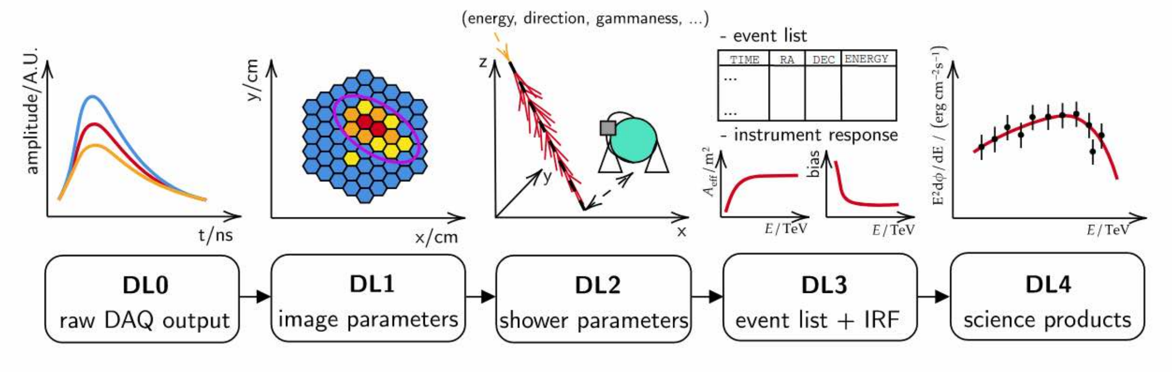

FIGURE 1.4: A schematic representation of the steps in the data analysis chain of IACTs. Low-level work such as that of direction reconstruction involves data products from DL0-1 whereas Gammapy utilizes DL3 products [17].

1.3.1 Shower Simulations

Pioneered by the Whipple collaboration in the 1970s, *Monte Carlo* (MC) simulations of EAS are crucial in the development of IACTs and the processing of the data generated therein. In the absence of direct calibrations, they provide a way to estimate the telescope performances and present critical inputs while building such telescope systems. The steady increase in computational power over time has allowed the creation of ever larger and more realistic simulations. Now, it is common practice to test all changes to the data analysis and their impact on the system's sensitivity using simulated events [6, 5].

The input parameters to current state-of-the-art shower and telescope simulations, such as the *CORSIKA* and *sim_telearray* suites currently used in H.E.S.S., take

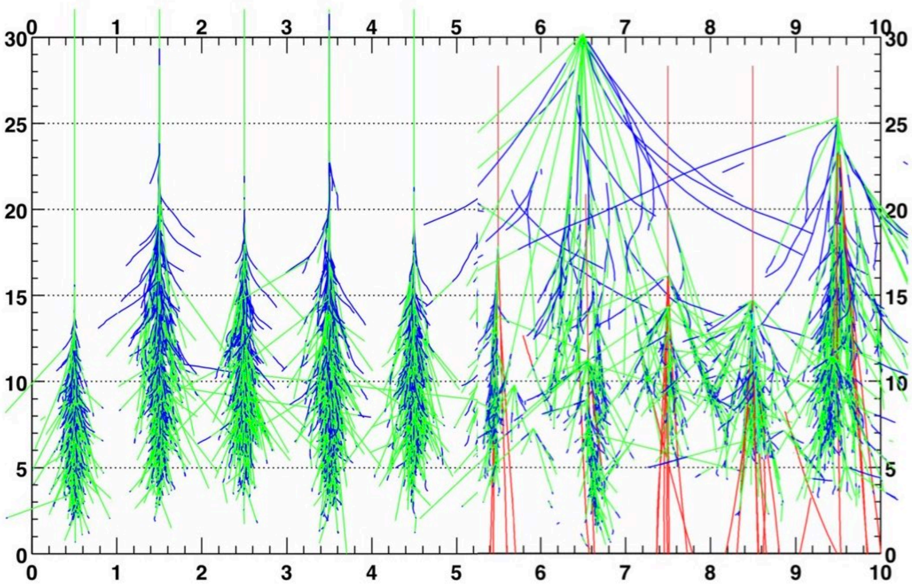

FIGURE 1.5: Illustration of the intrinsic variability of EAS through MC simulations: the five showers on the left have 300 GeV γ-ray photons as seeds and each of the five on the right are initiated by protons of the same energy. The y-axis is the shower height in km. The figure is adapted from [6].

into account the various factors that affect shower development, including shower interaction and atmospheric profile models, the effects of the Earth's geomagnetic field on the charged particles, the characteristics of the telescope system itself, as well as observation site-specific details (the altitude for instance) [18, 8]. Figure 1.5 shows the side profiles of ten such simulated air showers.

As an output, the Cherenkov image of the simulated EAS detected by the telescope(s) is recorded. These images can be manipulated and studied in much the same way as real images of air showers, thereby tremendously aiding testing and improvements to be made to the data processing pipeline.

1.3.2 Low-level analysis

Once an event triggers and is recorded by an IACT camera, the raw data is in the form of binary files that contain the sampled waveform at all camera pixels (PMTs), which represents the captured image. Taking into account factors such as the efficiency of each pixel, broken PMTs and electronics responses, this raw data is reduced to a list of quantities per pixel such as the charge (number of photoelectrons or p.e.) and photon arrival time.

The signal in these pixels, apart from Cherenkov photons, also include other photons not attributable to Cherenkov emission, such as those from stars and the moon as well as residual terrestrial light. This is called the *night sky background* (NSB). The next step, therefore, is *image cleaning* whereby the images are further processed to select only those pixels that recorded Cherenkov light. Either of two methods are employed for this: (i) *tailcuts cleaning* which selects for spatially correlated features in the recorded image [19] and (ii) *time cleaning* which selects for features which are both spatially and temporally correlated (unlike NSB noise) [20].

At this stage, the pixelated shower image, representing the distribution of Cherenkov light in an EAS (Figure 1.6a), can be parametrized using the moments of its measured distribution (effectively approximating as an ellipse) and its position on the camera. These image parameters are termed the *Hillas parameters*, some of which can be seen in Figure 1.6b [21, 19].

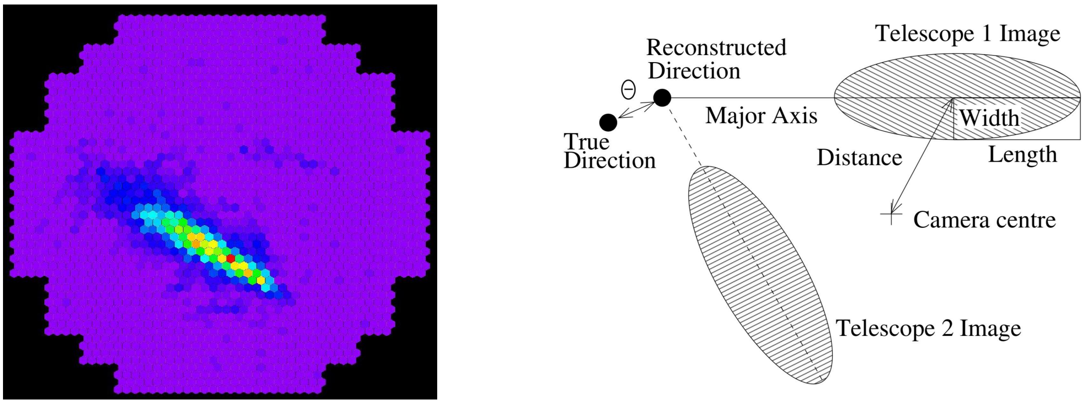

(A) γ-ray event seen by CT5 [14]

(B) Hillas parameters [19]

FIGURE 1.6: First stage of low-level data analysis in H.E.S.S.: after cleaning, a γ-ray event (a) can be approximated as an ellipse to get the Hillas parameters (b).

In addition to the geometric parameters such as length, width, etc., other information like the number of photoelectrons detected by the camera (image amplitude), time of triggering of the PMTs and total number of pixels in the image is also saved.

γ-hadron separation (GHS)

As already introduced, an overwhelming background of CRs also produce EAS and their events need to be filtered out in order to detect a γ-ray signal. The intrinsic differences in the shower production for hadronic and photon seeds is well-studied through MC simulations (Figure 1.5) and can be used to distinguish between these two types of events. *Boosted decision trees* (BDTs) are most notably utilized for this step – an event's Hillas parameters are used to classify it as either γ-like or hadron-like [22]. This step is also referred to as *event selection* or *background rejection*.

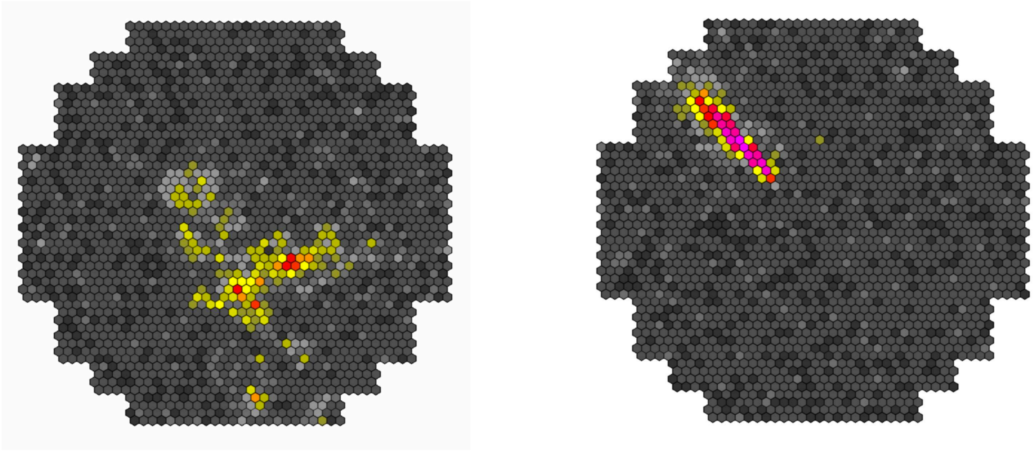

(A) CR event

(B) γ-ray event

FIGURE 1.7: The shape of the camera images of (a) CR and (b) γ-ray EAS help in distinguishing between them and filtering out the CR as background. The events are as seen by CT5. Picture credit: [11] and the H.E.S.S. Collaboration.

GHS in the case of events seen only by CT5, the so-called *mono observations*, suffers. In the case of stereo observations (involving CT1-4), events recorded by multiple telescopes are better constrained – the Hillas parameters of individual telescopes are averaged and reconstruction information from all telescopes are available. For mono events, only the image parameters are available for separation.

Event reconstruction

At this stage, usually after GHS has taken place, a list of *γ-like events*, with their corresponding shower information such as the energy, direction and core location on the ground, can be obtained. This step is called *event reconstruction*.

For stereoscopic observations, as illustrated in Figure 1.8, a purely geometric 3D reconstruction of the direction of the EAS is made possible by combining images from multiple telescopes. This method is also called *Hillas-based reconstruction* [23]. For the current generation of IACTs, a sophisticated method called *ImPACT* is used [24]. In this technique, the shower parameters (energy and direction) are obtained by fitting shower images with shower templates obtained from MC simulations.

For mono observations, on the other hand, the lack of a stereoscopic view leads to a less precise determination of the primary particle's direction. For further details regarding the current mono reconstruction techniques, see Chapter 2. Improving the angular reconstruction for mono observations, which forms the premise for this thesis work, and the implementation of these techniques is discussed in subsequent chapters.

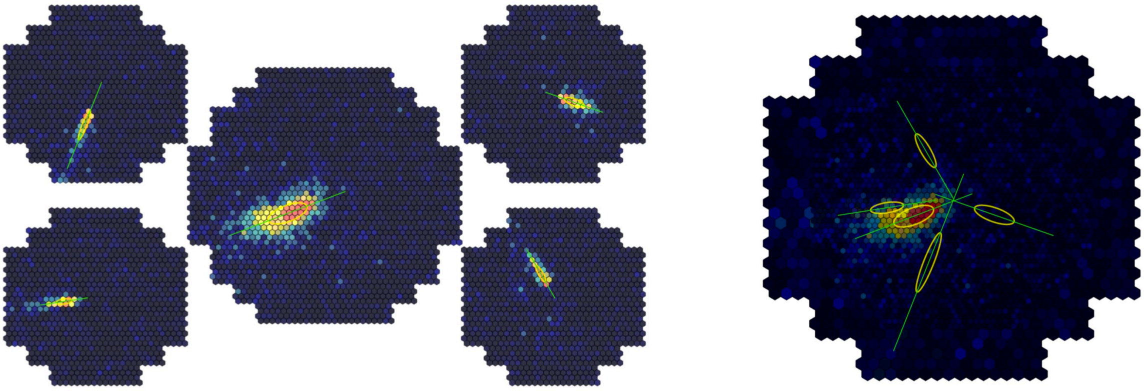

(A) Stereoscopic view (B) Stereoscopic reconstruction

FIGURE 1.8: A simulated 700 GeV γ-ray event as seen by the five telescope cameras of H.E.S.S. II (a). Intersecting the major axes of all five events is used to determine the direction of the shower (b). Picture credit: [11] and the H.E.S.S. Collaboration.

1.3.3 High-level analysis

The data products involved in high-level analysis are independent of the detection techniques as well as calibration and analysis methods (DL3, refer to Figure 1.4). These data products consist of: (i) a list of reconstructed γ-ray events (referred to as “events” from now on), and (ii) their corresponding *instrument response functions* or *IRF*s. IRFs represent the responses of the telescope system and therefore allow the determination of flux points, signal significances, etc. from the measured γ-ray signal. These include the effective area and exposures, residual background from GHS and reconstruction (angular and energy) accuracies.

Note that IRFs will reflect any changes brought on by improvements in previous stages of data analysis. The point spread function (PSF), for example, represents the direction reconstruction accuracy and any upgrade to the angular reconstruction capabilities will be reflected through this function.

Gammapy

Gammapy is an open-source, Python-based software package widely utilized in the high-level analysis of data from IACTs. It employs standard Python packages such as Numpy, Scipy, Astropy and matplotlib. Gammapy is used to obtain a variety of science products such as light curves, flux and significance maps as well as spectral fits to observational data available in the form of γ-ray event lists and IRFs [25, 26].

This software package is used consistently throughout this work, when setting the benchmark cases and when later evaluating the improvements made to the analysis pipeline. The details about specific methods utilized for this thesis and the resultant science products are disussed in later sections.

1.4 VHE sources: γ-ray Active Galactic Nuclei (AGN)

Much of the radiation propagating in the universe is thermal in origin, such as that generated in stars and hot gas [27]. However, certain radiation components result from non-thermal processes, which is made clear by their energy spectra, showing no indication of a black body origin, and their energies that go well-beyond what is possible through thermal mechanisms. An important class of astrophysical sources showcasing broad-band, non-thermal spectra that are sources of VHE gamma-rays, and therefore have been demonstrated to be sights of particle acceleration, are *active galactic nuclei* (AGN) [28, 29, 30].

Active galactic nuclei, as the name suggests, are astrophysical sources located in the centres of some galaxies. They are powered by accretion into the central *supermassive black holes* (*SMBH*) of the host galaxies. Their luminosities are well beyond that of "normal" galaxies, making them visible upto very high redshifts [31]. Detectable emission from these sources covers the whole electromagnetic band and make them ideal candidates for multi-wavelength studies [32].

Various classification schemes attempting to categorise these sources based on the observed various phenomenological differences were proposed. However, now it is of general consensus that a *unified model* is a more plausible answer. According to this model, various observational differences arise due to differences in the orientation/inclination of the AGN with respect to the line of sight of the observer [34, 33, 30].

The present, approximate structure of an AGN that arises out of the unified model is illustrated in Figure 1.9). The figure also shows the various AGN classes adopted over the years.

1.4.1 Blazars and their subclasses

Blazars are a special class of AGN that contain jets aligned very close to the line of sight (LoS) of the observer ($< 10^\circ$). This orientation of the jets allows for the emission to be highly Doppler-boosted, making them dominant emitters in the γ-ray sky despite their relative rarity. Blazars are characterised by their compact radio cores, continuum emission, rapid variability (detected as flares) and high degree of

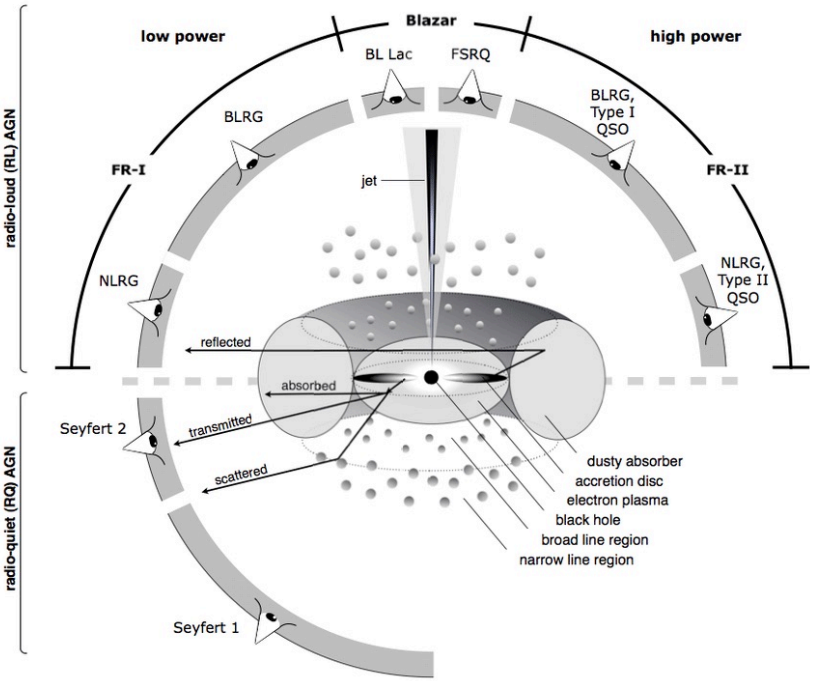

FIGURE 1.9: **Structure of an AGN**: the central SMBH is surrounded by an *accretion disk* (optical/EUV emission) with a 'corona' of electron plasma residing above it (X-ray emission). An IR-emitting dusty *torus* surrounds the whole accretion disk structure. Clouds of gas move in close proximity to the SMBH (*broad line*) as well as beyond the torus (*narrow line*). Collimated *jets* of relativistic particles may also be beamed along the poles of the disk. Note that the main difference between the classification of an AGN as a radio galaxy or blazar depends on the angle of viewing the jet. Picture credit: Marie Luise Menzel [33].

polarisation [34]. These objects are therefore particularly important in the study of jet dynamics, accretion processes and high-energy radiative phenomena.

They can be divided into two main sub-classes: (i) *BL-Lacs*, which lack strong emission or absorption features in their spectra, and (ii) *Flat spectrum radio quasars (FSRQs)* which showcase broad emission lines [34].

1.4.2 Spectral Energy Distributions (SEDs)

The multiwavelength *Spectral Energy Distributions* or SEDs of most blazars show a characteristic double-humped shape as shown in Figure 1.10. Peaking in the IR to X-ray bands, the lower-energy component is usually attributed to synchrotron radiation from relativistic electrons in strong magnetic fields. The origin of the higher-energy component is thought to be due to a combination of Inverse Compton (IC) on the synchrotron photons (Synchtrotron self-Compton or SSC) or external thermal photon field as well as hadronic processes [3]. Note that the downturn in the second hump occurs in the VHE regime, thereby making it important to study these sources at these energies.

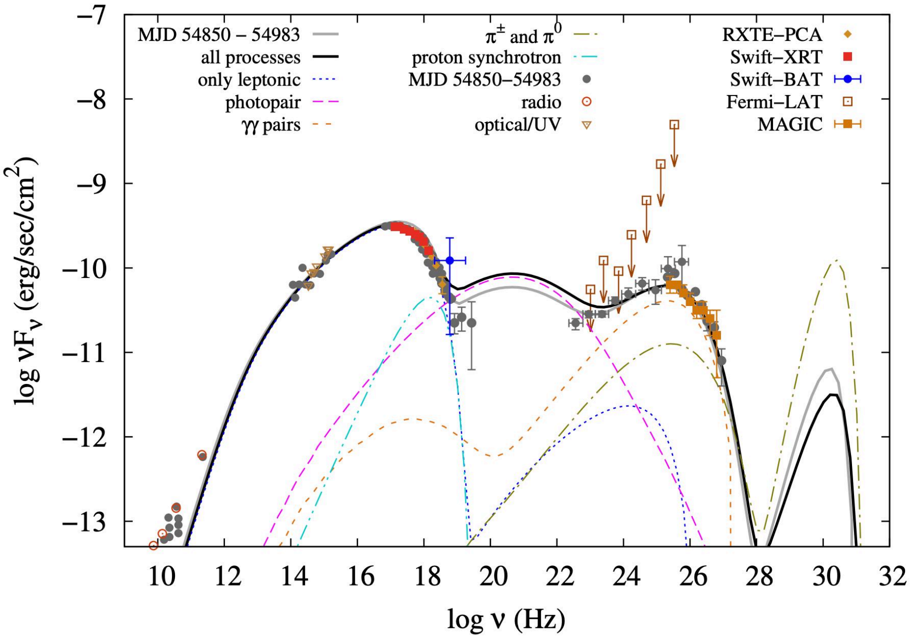

FIGURE 1.10: The multiwavelength SED of the BL Lac Markarian 421 (the first extragalactic source of VHE energy to be discovered [35]) during a flare in 2010 [36]. Observations with H.E.S.S. (not shown here) would roughly correspond to the range of MAGIC (filled orange squares). Note that the various coloured lines represent the various components of the model fits proposed by the authors. The third hump at 5-10 PeV arises because the EBL absorption has not been taken into account.

1.4.3 Extragalactic Background Light (EBL) and its estimation

The *extragalactic background light* (EBL) traces the star formation history of the universe, and represents the UV through IR emission from stars, galaxies and AGN. It is very important in the cosmological context, being the second-most energetic diffuse emission after the *cosmic microwave background* (CMB) [37]. The overwhelming local foreground light makes direct measurements of EBL very difficult but its intensity can be characterised indirectly by studying the γ-ray spectra of sources across various redshifts [37, 38, 39].

γ-rays interact with EBL photons via pair-production— the higher the energy of the γ-ray, larger is cross-section of interaction. As a result, the spectrum of a γ-ray source at a given redshift displays a steepening or cutoff at TeV-scale energies. The

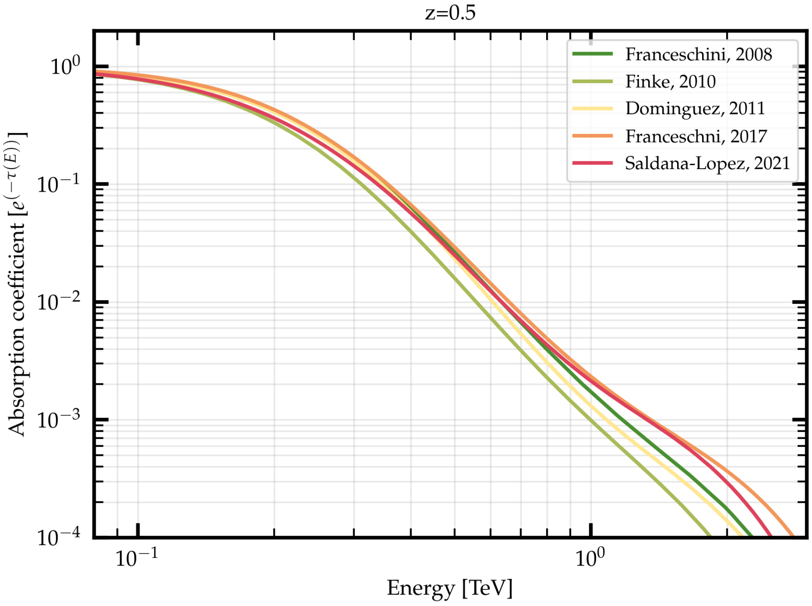

FIGURE 1.11: Various models of the EBL absorption coefficient/factor for a source at redshift of 0.5. These are available as built-in versions on Gammapy; the scaling factor α has been set to 1.

EBL absorption factor is given by

$$exp(-\alpha \times \tau(E, z)) \tag{1.4}$$

where $\tau(E, z)$ is the *optical depth* predicted by a model and α is a *scaling factor* for the optical depth [40]. Hence, by measuring this degree of absorption imprinted on the spectrum, the intensity of EBL present in intergalactic space can be probed. Various EBL models are plotted in Figure 1.11.

Chapter 2

Event Reconstruction in H.E.S.S.

For H.E.S.S. mono observations, due to the unavailability of a steresocopic view, it is difficult to reconstruct the direction of arrival of the primary γ-ray. This, however, can be bettered through the use of more event-specific parameters and reliable techniques for reconstruction, the development of which is the aim of work presented in this thesis.

This chapter provides an overview of the analysis pipeline utilized for this work and the inherent flaws in the current analysis method. The alternative use of “event classes” in place of the present approach is discussed, alongside the special class involving only mono events. The new parameters employed for building on the ongoing direction reconstruction are also discussed briefly.

2.1 The H.E.S.S. Analysis Pipeline (HAP)

The H.E.S.S. collaboration has developed multiple pipelines for data analysis. These are used in the calibration and data reduction of H.E.S.S. observations as well as simulation-based tests. The presence of multiple pipelines allows the cross-checking and ensures the robustness of obtained results.

The *H.E.S.S. analysis pipeline* or *HAP* is the software pipeline version used in this work. It comprises several software modules, primarily written in C++ and Python, maintained throughout internal H.E.S.S. servers and exploited for various tasks along the analysis chain (Section 1.3). Given a list of observation (or simulation) runs with raw DL0 data, HAP can be used to obtain cleaned and parametrized events to be further exploited, either for source analysis or to carry out algorithm improvements.

ROOT framework

HAP inputs are provided in the form of ROOT files. ROOT is the main software framework used in high-energy physics for data analysis [41]. For supervised machine learning techniques employed in the analysis chain, such as BDTs for GHS and artificial neural networks for event reconstruction, HAP utilises the Toolkit for Multivariate Analysis (TMVA) ROOT library [42].

2.2 Current approach and shortcomings

At present, the default scheme implemented for H.E.S.S. data analysis involves selecting a particular set of telescopes whose data are then used for analysis. The possible configurations are: (i) only the central telescope (mono), (ii) the four smaller telescopes (stereo), and (iii) all five of them (hybrid). The problem with this scheme is that the energy range accessed is artificially limited by apriori choosing such a configuration, as can be seen from the effective area curves in Figure 2.1. For a given observation (in which a number of events of are registered by the telescopes), the effective area is limited to one of the curves.

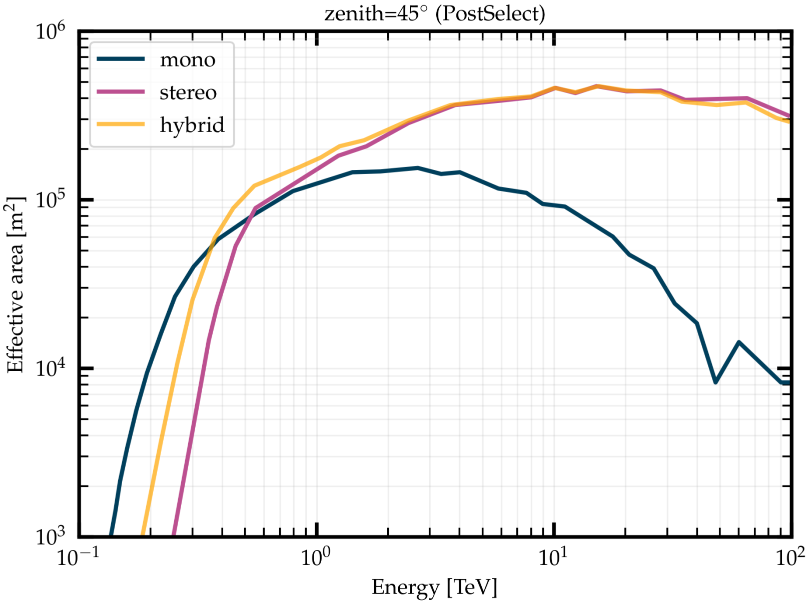

FIGURE 2.1: The effective areas for the three different analysis configurations for events at 45° zenith (a similar behaviour is seen at other zeniths as well). Note how by choosing either the hybrid or stereo arrangements, the access to low energy events and vice versa, is hampered. Picture credit: Rodrigo Guedes Lang (H.E.S.S. collaboration meeting, 2022)

Note, however, that this approach is not always avoidable. While dealing with observations taken during the H.E.S.S I era or when not all five telescopes are functioning, for instance, the telescope configuration used for analysis needs to be decided beforehand.

2.3 Event classes

A uniform framework of data analysis is required to exploit the full energy range of the experiment and get rid of discrepancies between the two experiment phases (H.E.S.S. I and II). This can be achieved by dividing events, based on their quality, into complementary and but independent *"event classes"*. Based on the amplitude and number of telescopes triggered (n), an event can fall into one of the following classes:

- **Class A**: Amplitude(CT5) > 50 p.e. *and* n(CT1-4) $\geq$ 2, with amplitude > 200 p.e. for all
- **Class B**: Amplitude(CT5) > 80 p.e. *and* either n(CT1-4) $\geq$ 1 or n(CT1-4) $\geq$ 2, with amplitude $\geq$ 80 p.e.
- **Class M**: Amplitude(CT5) > 100 p.e. *and* no triggered CT1-4 telescope has amplitude > 100 p.e.
- **Class C**: Very low-quality and neglected

Event classes are beneficial because they allow an optimisation of the analysis for each class. The classes can then be jointly considered in the final analysis. An implementation of this framework, therefore, requires a good understanding of each telescope's reconstruction capabilities. The advantage of the event classes over the current default configuration technique can be seen in Figure 2.2. Note how a much better energy and effective area coverage for a given observation is obtained by combining the individual performances.

Therefore, event classes allow the combination of events from different telescopes and the information they hold about the primary γ-ray. With better reconstructed events at lower energies, the obtention of which is the aim of this work, the usage of event classes can help bring down the systematic errors associated with the angular resolution, and energy bias and resolution. When dealing with real-world observations, these systematic errors are reflected through the IRFs (Section 1.3.3).

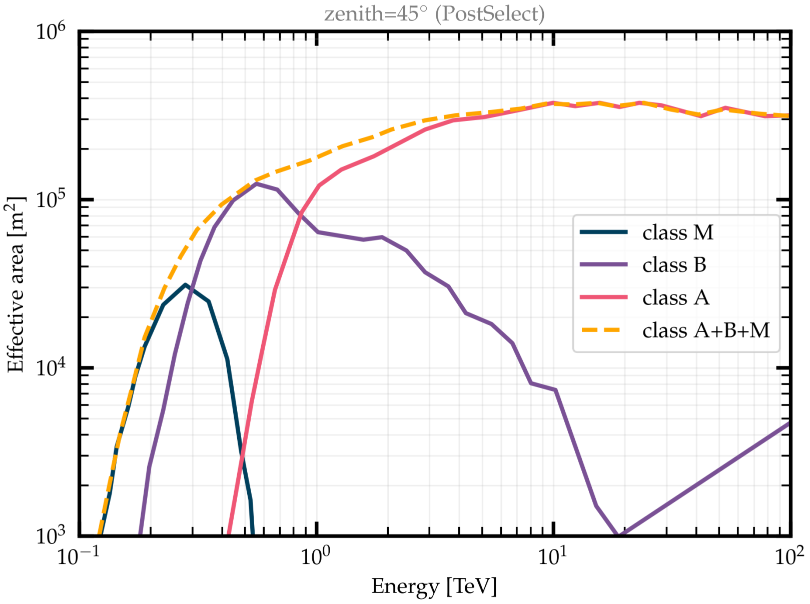

FIGURE 2.2: The individual and combined effective areas of the three event classes for events at zenith=45°. Note how low energy events can now be accessed in a single observation. Picture credit: Rodrigo Guedes Lang (H.E.S.S. collaboration meeting, 2022)

2.3.1 Class M or mono

Since CT5 has the largest energy range and lowest energy threshold of the H.E.S.S. telescopes, the M event class becomes particularly important. Low-energy events are often only detected with CT5, making it necessary to perform a monoscopic reconstruction. Therefore, in order to effectively utilize the whole energy range of the experiment, improving the accuracy of the data analysis involving this telescope is a must.

Recall that in stereoscopic reconstruction, intersecting the major axes of shower images from multiple cameras allows the accurate determination of the shower direction (Section 1.3.2). For mono events, however, the direction of arrival of the primary γ-ray is difficult to ascertain with just the Hillas parameters – it could lie on either end of the major axis as shown in Figure 2.3. This ambiguity is partially solved by considering the skewness of the image, which is a proxy for the asymmetry of the shower image distribution. The current event reconstruction scheme uses this skewness parameter for determining the direction.

However, for low-energy events of the order of a hundred GeV, which CT5 is most sensitive to, only a handful of pixels in the camera are triggered and it becomes increasingly difficult to decipher the original direction. As a result, the current analysis method is limited by systematic uncertainties arising from this degeneracy.

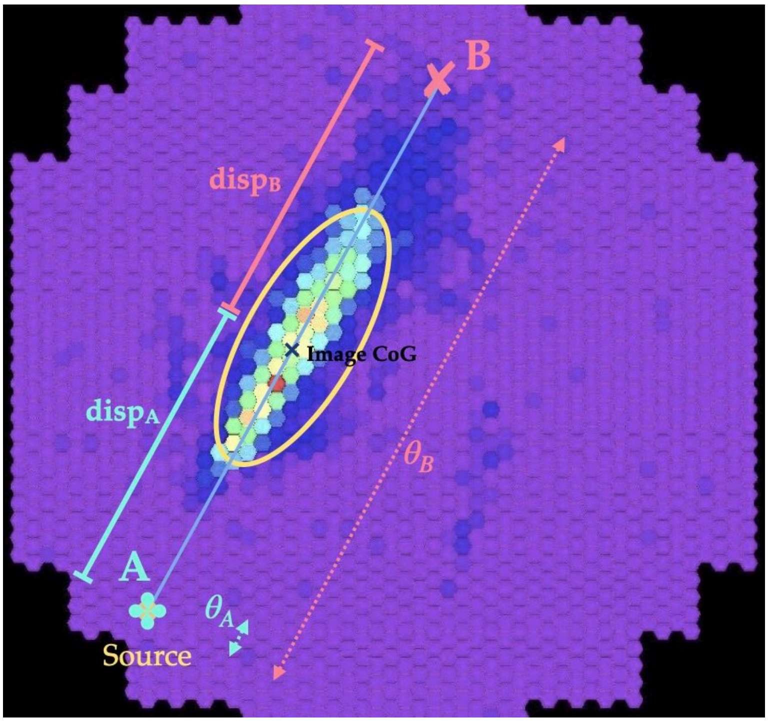

FIGURE 2.3: **Degeneracy in the direction reconstruction**: for the same value of disp (distance between image centre and direction of primary γ-ray), the reconstructed direction can lie on either side of the major axis (A or B). For events whose directions are correctly determined, the value of θ is reasonable (θ_A) but for the wrongly reconstructed events, the value of θ is way off (θ_B).

Event reconstruction of CT5-only events (mono reconstruction)

Event reconstruction (as outlined in Section 1.3.2) is a two-fold process, involving the determination of both the energy and direction of the primary γ-ray. For mono events, this step is split into two tasks:

- **Regression task**: a neural network is used to reconstruct the energy and *disp* – the distance of the image CoG to the actual direction of the incoming γ-ray (Figure 2.3).
- **Classification task**: the side of the major axis on which the true position of the primary γ-ray lies is discerned by looking at the image skewness.

Although skewness predicts the correct side for most events (the shower direction of more than 80% of events above 250 p.e. are correctly determined), the calculating an incorrect side leads to a very large displacement from the true source position. The angular separation of the reconstructed position from the true position (side, that is) is given by θ; for the wrong recontructed position θ is large (see Figure 2.3).

2.4 The new image parameters

To help address the degeneracy in angular reconstruction, a set of other complementary image parameters are defined using the timing and charge information of an event. These include: (i) the **time gradient** (based on the arrival time of the Cherenkov photons in different sections of the ellipse), (ii) the **charge asymmetry** in the image and (iii) additional geometric parameters obtained by sectioning the ellipse into 3 sectors, like each sector's center of gravity (CoG; x_0-x_2) and **amplitude-weighted width** (w_0-w_2). The new image parameters are visualised in Figure 2.4 and are part of the new generation of MC simulations to be used in H.E.S.S. The definitions of these new parameters can be found in Table 4.1.

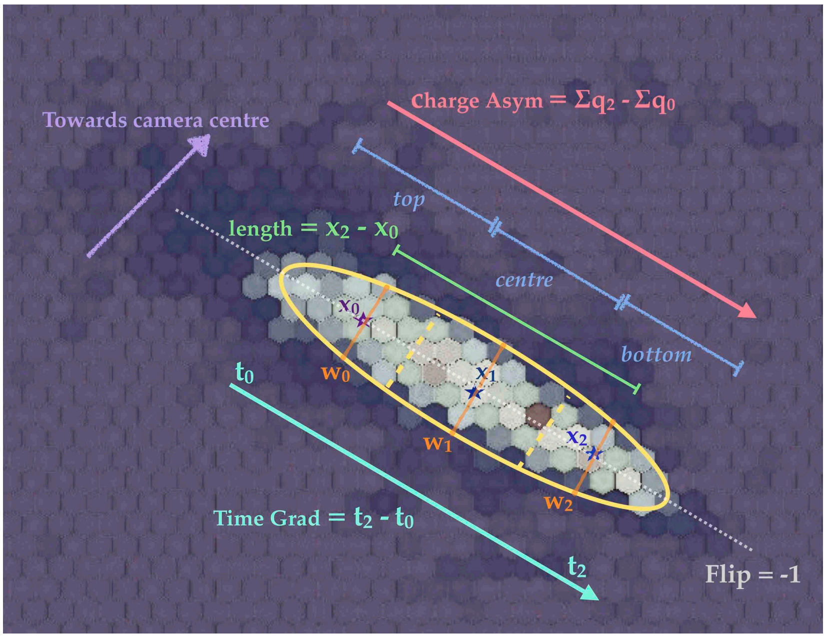

FIGURE 2.4: The new image parameters: the Hillas ellipse is divided into three sectors (top, centre and bottom). x_0-x_2 are the sector CoGs and w_0-w_2 are the amplitude-weighted widths of each sector. Other parameters relevant to this work, such as the flip, are also illustrated.

For simulated events, the true source position is known and a variable to indicate this can be defined– the variable "flip" can have values of +1 or -1, depending on which side of the ellipse major axis the true position lies. It is calculated in the local frame of the telescope's camera for MC simulations and is dependent on the which part of the camera the event lies on. Note that the value of the flip is used to calculate the true position and does not directly represent the position (-1 for instance, is not a position).

It is very important to note that events are not "classified" into two flip classes of +1 or -1. The flip value is representative of the event's direction and all comparisons need to be made with regards to whether the value (and therefore position) has been correctly predicted for a given event and not between events with different flip values.

Improving the angular reconstruction of mono events

A neural network can now be trained to execute the (classification) task of determining the direction using the flip of each event as the label. Along with information from the image asymmetry (skewness) and tailedness (kurtosis), taking into account a combination of the aforementioned new parameters to reconstruct the direction can be crucial in finding a way to reduce the degeneracy in the direction reconstruction algorithm.

Chapter 3

Artificial Neural Networks

Machine learning or ML, is the science of programming computers to learn from data. A variety of ML systems are currently employed to solve a multitude of tasks involving big data that are deemed too complex for traditional approaches such as image classification and speech recognition. They help provide insights into non-trivial problems, and serve as powerful computational tools easily adaptable to changing conditions (in the form of changing data) [43].

Motivated from the design and organisation of biological neural networks found in animal cerebral cortexes, artificial neural networks (ANNs) are powerful ML tools commonly employed for classification and regression problems. This chapter broadly discusses the concept of ANNs, the data used and introduce the Python libraries employed for this study.

3.1 Supervised machine learning

A major class of ML systems is based on whether they are trained with human supervision. In the case of supervised ML, computers learn from data labelled with true values. ANNs are a subset of supervised ML and are trained on labelled data to identify relationships and patterns among the inputs parameters that may otherwise not be easily discernible to the human eye or modelled in a simple manner.

With the advent of large computational resources, improvements in training algorithms and availability of large quantities of data for training and testing, ANNs are widely used to tackle large and complex ML tasks, such as image classification [43].

3.2 Training and testing datasets

In the context of this project, the training dataset is a new generation of MC γ-ray shower simulations as seen with H.E.S.S., and cleaned and parametrized with with HAP. The energy, true direction and other reconstructed image parameters and their distributions (including that of the new ones described in Section 2.4) are well known. These MC parameter values are the labels of the data. For this work, given a set of reconstructed event parameters, ANNs are used to carry out two tasks : (i) to obtain the energy and disp values and (ii) determine what flip is needed for direction reconstruction. The MC shower simulations are of two types:

- **Fixed offset (FO)**: For a given *zenith* and *azimuth* angle of observation, the position of the point-source is fixed at a given directional *offset* and a variety of events with different energies are simulated. Note, however, that the source is offset to only one side of the telescope pointing direction.
- **Diffuse**: Events are simulated for a given zenith and azimuth randomly across a wide range of offsets. Although more realistic, diffuse simulations are highly computationally expensive to obtain. This also means that for a given offset band, the number of events are much lower than that for FO simulations. For the purpose of this thesis, they are primarily used to carry out checks on the ANN performances and accuracy of direction reconstruction.

For testing purposes, an independent and randomly chosen subset of the MC simulations is used. The final testing is carried out on actual H.E.S.S. data (observations of two AGN, discussed in Chapter 5).

3.3 Components of an artificial neural network (ANN)

Artificial neurons are modelled in much the same way as biological ones. The simplest one, called a *perceptron*, comprises a node (the neural body) that receives one or more binary inputs (synapses) and produces a single binary output (the axon) [43]. The *sigmoid neuron*, which is the advanced and more practical version of the perceptron, takes in inputs that have continuous instead of binary values. Henceforth, any reference to a neuron would allude to the sigmoid neuron.

Consider the simple case of a single neuron getting its input from a set of other neurons (Figure 3.1). To obtain the output from this neuron, a weighted sum of all the inputs is taken; the *weights* serve as indicators of how much the input matters to the neuron in question. This value can then be shifted using a *bias* associated with this neuron. The final output from this neuron is then obtained by applying the *activation function*, which decides whether the neuron should be activated (provide valuable inputs to succeeding neurons) and if yes, how large of a contribution to the network it should have.

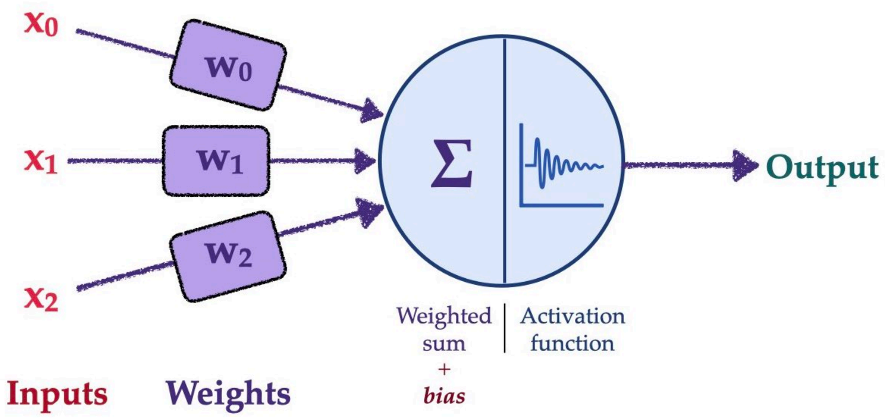

FIGURE 3.1: A simple sigmoid neuron that takes 3 inputs and outputs a single value. Figure adapted from [43].

3.3.1 Deep Neural Networks

A *deep neural network* (DNN), which is used in this work, has several neurons arranged in layers (refer to Figure 3.2). It necessarily contains (i) an *input layer* made of neurons to which a list of input values can be fed (in this case, the image parameters) and (ii) an *output layer* which, depending on the requirement, consists of one or more neurons. The values of the output neurons could be actual predictions (in the case of regressors) or class probabilities (in the case of classifiers). Connecting these two layers are the so-called *hidden layers*, arranged in much the same way as any neuron layer.

The output of a neuron in the k'th layer of a DNN is given by:

$$o_{jk} = A_{jk}(\sum_i [w_{i(k-1)} \times x_{i(k-1)}] + b_{jk}) \tag{3.1}$$

Here, o_{jk} is the output of the jth neuron in the kth layer and A_{jk} is its activation function. All the inputs from the previous $(k-1)$th layer (the x_i's) are multiplied with their corresponding weights (the w_i's) and summed over. The shifting of the activation function can be adjusted using the bias for that output neuron, called b_{jk} [44], [45].

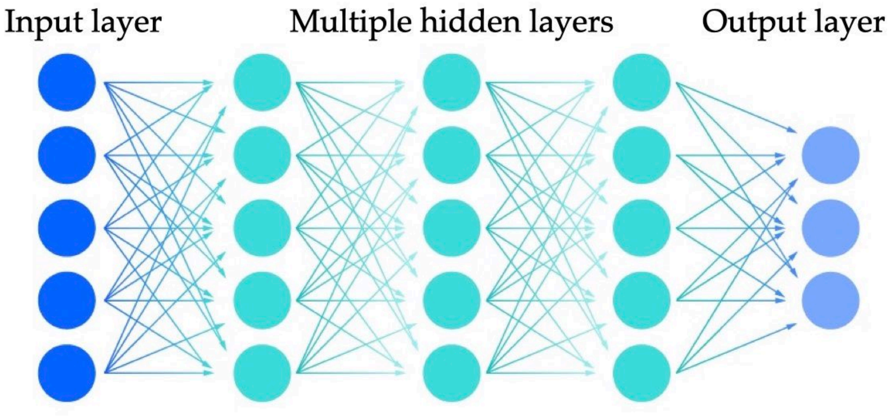

FIGURE 3.2: A simple deep neural network (DNN) with an input layer of 5 neurons, an output layer of 3 neurons, and 3 hidden layers with 5 neurons each. The arrows indicate the weights of the network. Figure adapted from [46].

Loss function and training

The values from each neuron in the output layer can be compared to the actual/true values, i.e., the labels of the data. The accuracy of a NN model can then be evaluated with the *cost* or *loss function*, which quantifies how different the predictions of the NN are from the actual values. It is a function of all the weights and biases. There are several loss functions, a common one being the *mean squared error*:

$$C(w,b) \equiv \frac{1}{n}\sum_{\mathbf{x}} \parallel y(\mathbf{x}) - \mathbf{a}(w,b,\mathbf{x}) \parallel^2 \tag{3.2}$$

Here, $\mathbf{x}$ represents the set of input parameters for a given training event. $y(\mathbf{x})$ is the true value(s) and $\mathbf{a}(w,b,\mathbf{x})$ is the vector of model-predicted values for a given $\mathbf{x}$. The loss function is calculated for each training instance being fed to the ANN. However, since there are usually millions of data points to train on, the loss is computed as an average for a set of (n) training examples, called a *batch* (hence the $\frac{1}{n}$). Other loss functions are similarly structured.

The method of *gradient descent* is employed to carry out the minimisation of the loss function. The weights and biases are updated as:

$$w_k \rightarrow w_k' = w_k - \eta\frac{\partial C}{\partial w_k} \tag{3.3}$$

$$b_l \rightarrow b_l' = b_l - \eta\frac{\partial C}{\partial b_l} \tag{3.4}$$

Here η is a small, positive parameter called the *learning parameter* and C is the loss function [45].

The *backpropagation algorithm* is utilised to adjust the weights and biases in a manner that leads to the convergence of the cost function to a local minimum. There are three main steps involved, namely:

1. A **forward pass**, in which the neural network is used to make a prediction for a given training sample and the associated error (the value of the loss function, that is) is computed.
2. A **reverse pass** in which the error contribution from each layer is measured by going through each layer in reverse.
3. A **Gradient descent** step which tweaks the connecting weights and biases so as to reduce the error (Equations 3.3, 3.4)

A neural network architecture which involves the signal flowing in only one direction (inputs to outputs) is referred to as a *feed forward neural network (FNN)*. For computational efficiency, the training set itself can be divided into "batches" with *batch size* referring to the number of instances in each batch. The learning algorithm generally goes through the whole training set a given number of times, with each complete pass through the set called an *epoch*.

ANN hyperparameters

A large part of the power of ANNs arises from their inherent flexibility– numerous hyperparameters can be tweaked for the network to offer optimal results. The major hyperparameters that can be fine-tuned without the use of grid-search methods include the number of hidden layers and the number of neurons in each of them as well as the activation functions used for the neurons, the number of epochs and batch size [45].

For the first two, care must be taken to include not too many hidden layers or neurons in order to avoid overfitting the ML model on the training data, leading to worse generalization to the test data.. At the same time, smaller and shallower networks, although capable of providing very good accuracy in predictions, are unable to model complex functions as easily.

There are a wide variety of activation functions to choose from, the most common being the *sigmoid* or *logistic* function, *hyperbolic tangent*, *ReLU* and *swish* (Figure 3.3). Each has its drawbacks and advantages, which have to be considered while deciding the ANN architecture for the task at hand. Ideally, an activation function is differentiable at all domain points.

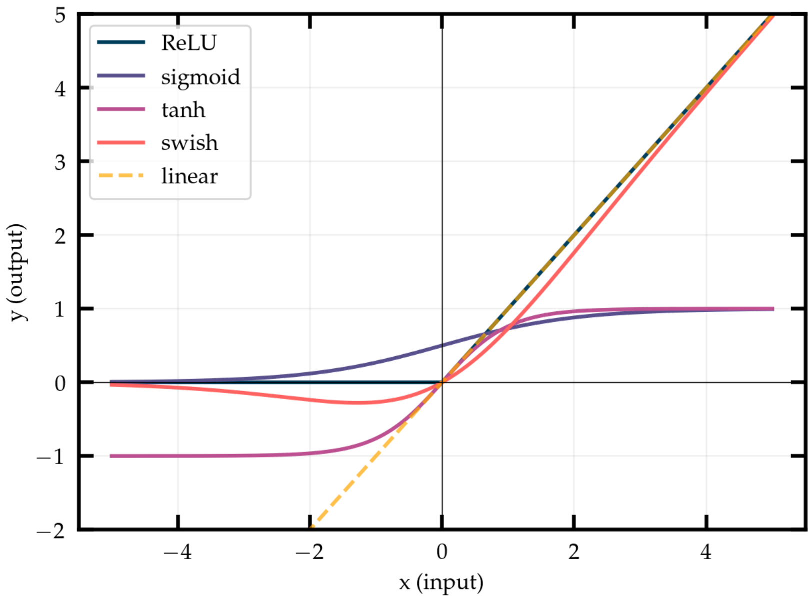

FIGURE 3.3: The most common activation functions used in ANNs. Note how, unlike the others, ReLU (rectified linear unit) is not differentiable at 0. Linear activation functions are typically used in the final neuron of regression tasks. For classifiers that deal with probabilities, the sigmoid function is utilized because the output lie between 0 and 1.

Finally, the epochs and batch size can be adjusted to make sure the gradient descent step converges in reasonable time.

3.4 Keras and Tensorflow libraries

Tensorflow is an open-source framework and library for ML that offers support for varied ML and deep-learning models, algorithms and numerical computations. Developed by Google and now maintained by a worldwide community of developers, it presents a Python-based front-end interface for training and deployment of ML models. It is easily adaptable to other languages and programming environments [47].

Keras acts as a Python interface for Tensorflow and is specifically designed as a library for deep learning tasks involving artificial neural networks. In particular, for this work, numerous implementations of ANN building blocks such as optimizers, dense layers and activations functions are obtained from Keras [48].

Chapter 4

Improving the event reconstruction capabilities for CT5

In this chapter, the results of the improvements carried out on the mono reconstruction techniques in H.E.S.S. are reported. It is found that using a neural network to determine the event direction outperforms the skewness method currently in place (refer to Section 2.3.1). Another neural network trained on the new generation of MC γ-ray simulations for the task of computing the energy and disp also performs reasonably and within good bias limits (< 15%). Following a brief outline of the structure of the simulation dataset, selection cuts and the neural network architectures employed for this work, the improvement of the angular reconstruction are discussed.

4.1 Methods

4.1.1 Simulations: training and testing sets

Out of the complete set of simulated γ-ray events at hand, 10^6 are randomly chosen to carry out the training, validation and testing of the ANN (the *preliminary* set). This preliminary set is divided into three parts once again: 70% of the picked events are used for training, 10% for validation and the remaining 20% for testing. The trained model is saved both as a Keras model (for evaluation purposes) and in the TMVA format (for later implementation in HAP).

As discussed in Section 3.2, simulated events can either be FO or diffuse. Training is carried out for each combination of zenith, azimuth and offset (or just zenith and azimuth for diffuse simulations) angles. The zenith and offset angles range from

0-60° and 0.0-3.0°, respectively and the azimuth angle is either 0° or 180°. There is no intrinsic difference in the training carried out for FO and diffuse simulations.

Furthermore, only a million events from a much larger set of simulations are utilized for the preliminary task of carrying out improvements. This ensures that two more stages of testing can be carried out using: (i) the rest of the dataset not including the preliminary set, and (ii) actual observational data from H.E.S.S (discussed in the subsequent chapter).

An important point to note here: while simulating the events, for a given zenith, azimuth and offset angle, more simulations are carried out for events with smaller impact distances because of computational efficiency. Therefore, each MC event has a weight associated with it, with higher impact events given more weight. These *event weights* needs to be considered while training and evaluating the neural network.

4.1.2 Selection cuts

Certain "selection cuts" are placed on the event images before and during the DL2 analysis wherein only those images satisfying specific criteria are allowed for further processing. For this work involving the mono reconstruction, two such cuts (applied to the images before reconstruction takes place) are considered while training: (i) **safe cuts** (events with amplitude > 250 p.e. and >10 pixels surviving image cleaning are selected) and (ii) **ultra loose cuts** (events with amplitude > 60 p.e. and > 6 pixels). Additional parameter cuts relevant to γ-hadron separation are also considered but are not of importance when considering the event reconstruction.

A further cut selecting only images for which the image centroid lies within 0.72 m of the camera center is applied. This ensures only images that are fully contained in the camera and not truncated at the edge of the field of view are considered. This cut is then flexibly reduced to 0.80 m for testing with HAP. The stricter cut during training ensures that the ANN is well-trained on good-quality events and fewer outliers.

4.1.3 ANN architecture

As previewed in Section 2.3.1, there are three ANNs employed in mono event reconstruction, one each for the energy, disp and flip. A variety of architectures, with differing hyperparameters and input parameters, were tested and in each case, the one with the best performance was chosen. The final ANN architectures (Figure 4.1) along with the input parameters (Table 4.1) for each network are detailed below.

Training was carried out for a batch size of 1000 and with a maximum of 10,000 epochs. An *early stopping criterion* was set while training to ensure the best computational efficiency: the loss was monitored with a *patience* of 200 epochs. Patience is the number of epochs with no improvements before training is stopped. In addition, the event weights are considered in the form of sample weights when training.

The energy-disp-impact (EDI) network

This ANN takes 8 inputs and outputs the energy, disp or impact through a linearly-activated output neuron. It has 2 hidden layers, each with 20 neurons and the sigmoid activation function. The loss function is the mean squared error (Equation 3.2). This is illustrated in Figure 4.1.

There are two points of importance here: (i) although described together as the regression task, the ANNs (and thus the TMVA weights) for energy, disp and impact are separate. The architecture of each type, however, remains the same. (ii) the impact ANN is not directly utilized by HAP for reconstruction. Rather, it acts as a checkpoint to make sure the preliminary evaluations of the network on the new simulations are reasonable.

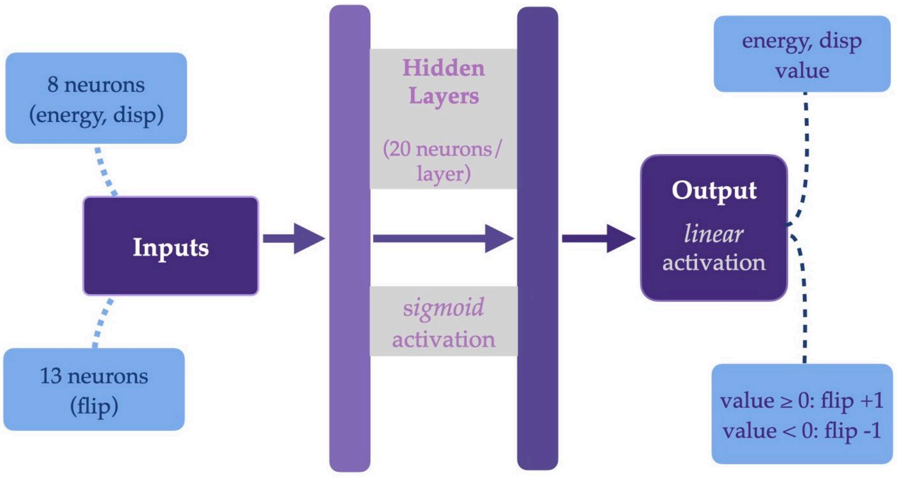

FIGURE 4.1: The neural network architecture employed for the energy, disp and flip networks used in this work. The basic architecture (shown in purple), comprising an input and two hidden layers and a single output neuron, remains the same for both tasks. The input parameters (summarised in Table 4.1) are different for each however and the two classes for the flip network are determined using a threshold cut at 0 which enables it to act as a classifier.

TABLE 4.1: Input parameters for the energy-disp and flip neural networks. The usual Hillas parameters employed in the present energy-disp network (without improvements) are shown in black. Along with the time gradient and charge asymmetry, they make up the 8 inputs for the new energy-disp network. In addition to these 8 parameters, the parameters shown in purple serve as the inputs for the flip network.

Hillas length	Semi-major axis length of the image ellipse
Hillas width	Semi-minor axis length of the image ellipse
Log amp	Log(image amplitude)
Log density	$\frac{\text{Image amplitude}}{\text{Hillas length} \times \text{Hillas width}}$
Skewness	Third central moment; measure of image asymmetry; Log(skewness) taken for energy-disp network
Kurtosis	Fourth central moment; measure of image tailedness
Time gradient	Difference in photon arrival times between top and bottom sectors
Charge asymmetry	Differences in produced charges between top and bottom sectors
w0 or width1	Amplitude-weighted width of the top sector
w2 or width2	Amplitude-weighted width of the bottom sector
Length	Distance between CoGs of the top and bottom sectors
Local Distance	Distance between the camera centre and CoG of the image
Npix	Number of pixels in the image

The flip network

The ANN used to predict the flip takes as input 13 image parameters, summarised in Table 4.1. It also has two hidden layers with 20 neurons, each having a sigmoid activation function. Just like the EDI network, the final output layer consists of a single neuron that is linearly activated. The loss function is the mean squared error. For it to act as a classifier, a threshold is set at 0. This ensures that values on either side of the threshold, that is ≥ 0 and < 0 are taken as either +1 or -1 respectively.

Classifiers with binary cross-entropy and a variety of activation functions were also tried and tested (the two output classes comprised -1 and +1 events). However, none performed as satisfactorily as the one described above (Figure 4.2).

4.1.4 Evaluation of the ANN performance

The performance measures for a regressor network (energy and disp) can be calculated using the distribution of the relative errors given by

$$\text{relative error} = \frac{\text{predicted value} - \text{true value}}{\text{true value}} \tag{4.1}$$

The *bias* and *resolution* of the regressor network is defined as the mean and standard deviation of this distribution, respectively. Their values are zero for a perfect predictor.

For a classifier, on the other hand, three important tools can be used to visualise the accuracy and performance:

- **the confusion matrix (CM)**: It is the 2D matrix-representation of the network's predictions. The simplest form of a CM is for the classification task involving two classes (or plausible output values), which also happens to be the task at hand. The two axes of the 2×2 matrix represent the true and predicted values. Figure 4.2 shows the confusion matrix of the current flip ANN and another trial classifier network at zenith = 20, and offset = 0.5.

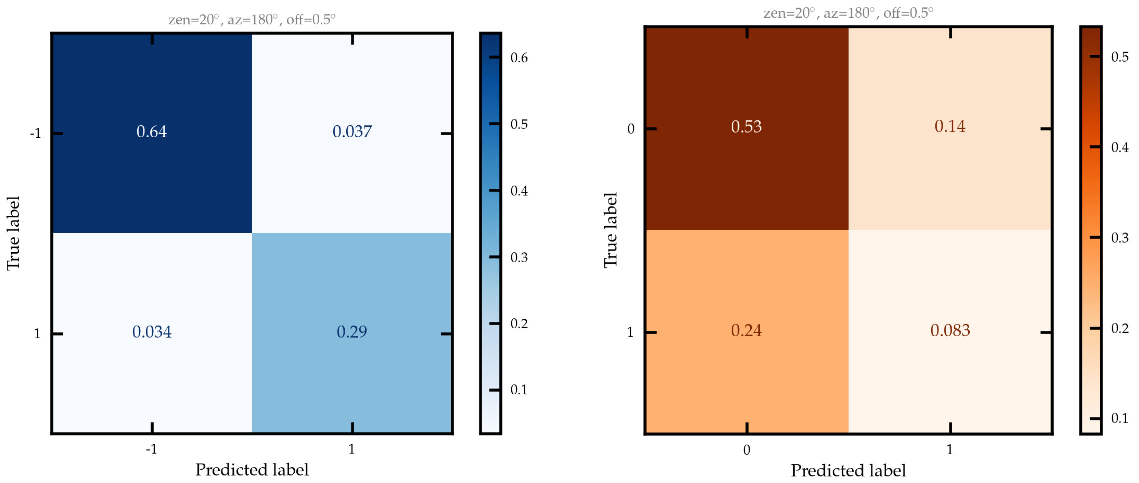

(A) A regressor-type classifier

(B) A classifier

FIGURE 4.2: The confusion matrix for (A) the final hybrid regressor-classifier network whose architecture is described in Section 4.1.3, and (B) one of the trial classifier networks (with swish activation functions for the hidden layers and the binary cross-entropy loss function). Note the different labels: for the latter network, the input classes are 0 and 1 corresponding to flip classes -1 and +1, respectively. The performance is very bad for the classifier, with an accuracy of 61.6%) compared to $> 93\%$ for the present, chosen network (A).

- **The bad flip fraction (BFF)**: For each (image) amplitude bin, the BFF is defined as:

$$\text{BFF} = \frac{\text{no. of wrongly flipped events}}{\text{total no. of events}} \tag{4.2}$$

  Here, "wrongly flipped events" refers to those events whose directions were incorrectly determined. Therefore, the same measure can also be used to check and compare the performance of the skewness method with that of the flip NN.

- **The θ^2 distribution**: The true direction (available from MC simulations) of each event can be compared with the direction predicted by the flip NN (or skewness). This offset angle θ, was described previously in Section 2.3.1 (See also Figure 1.6b). The unit of θ^2 is used because a constant solid angle on the sky per bin is maintained.

  Note that θ^2 distributions of the event counts in actual observations are also employed to check for the presence of a source at a known sky position (the true direction in this case). These are discussed later in Chapter 5.

4.2 Improvements to the monoscopic analysis

4.2.1 NN performance for energy

For CT5-mono, the energy range of interest is from around a few hundred GeV to around a few TeV. The bias of the energy network in this energy range is well within 15% as can be seen in the bias curves in Figure 4.3a. The corresponding energy resolution curves are shown in Figure 4.3b. The evaluation of the bias is carried out on the test set derived from the preliminary set.

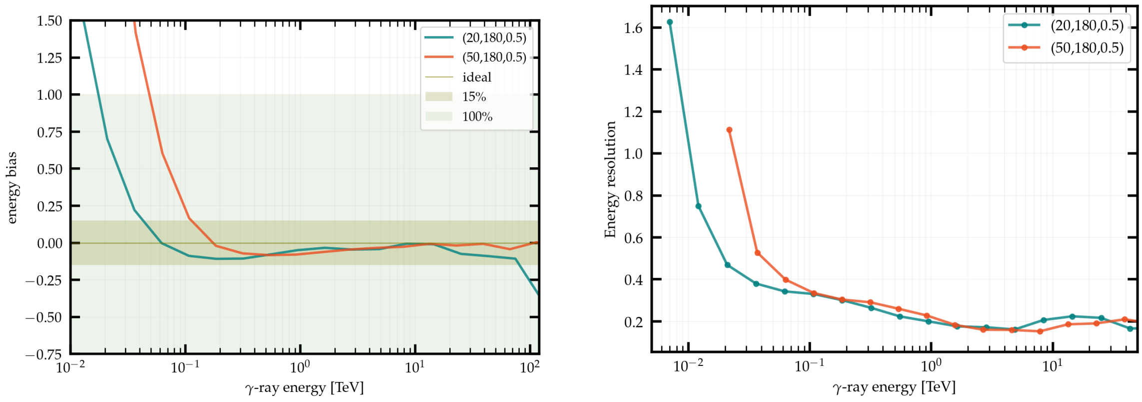

(A) Energy bias

(B) Energy resolution

FIGURE 4.3: The (A) energy bias and (B) energy resolution for neural networks trained on events at zenith = 20° and zenith = 50° for a fixed azimuth = 180° and offset = 0.5° (the zeniths and the fixed azimuth and offset are represented in the form of a 3-tuple in the label).The dark and light shaded regions in (A) represent the 15% and 100% bias ranges, respectively. Note that the bias behaviour at low and high energies as well as with zenith are as expected. The network biases and resolutions are within the 15% range and ≤ 0.4 respectively in the energy range important for mono.

The shape of the broad-scale energy-bias curve (Figure 4.3) is worth discussing: the over-prediction at smaller energies is because only those events with more than

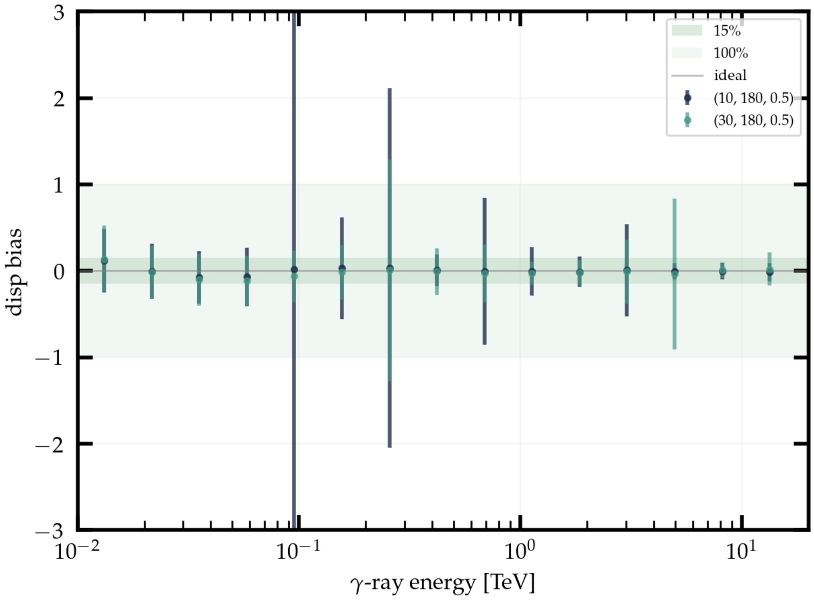

FIGURE 4.4: The disp network biases for zenith angles 10° and 30° (fixed azimuth = 180° and offset = 0.5°). The error bars represent the 1σ errors for each energy bin and therefore indicate the disp resolution. Once again, the network biases are within the 15% range for the energy range of interest for mono.

the average amount of light (upward fluctuations) trigger the telescopes and end up in the training sample. At higher energies, on the other hand, events are not fully contained within CT5 – the true image size of such an event is much larger than the detected one. This, therefore, leads to an under-prediction (negative bias). Furthermore, since the energy threshold of the instrument increases with zenith, so does the network's energy bias at low energies.

4.2.2 NN performance for direction reconstruction: disp and flip

Disp network

The disp network's bias lies well within 15% considering the energy range of interest for mono. The bias and resolution (seen through the 1σ error bars for the bias points) are shown in Figure 4.4. The large error bars in two energy bins for a zenith 10° are due to less events in the bin and a few incorrect predictions (large outliers). Note that a final, combined illustration of the direction/angular reconstruction is visualised through the θ^2 distributions (Figure 4.6).

The bad flip fraction (BFF)

The number, or rather the fraction, of bad flips per amplitude bin is obtained for the events in the preliminary test dataset by comparing the true and predicted directions. For the flip neural network this is just the number of events whose classes do not match. On the other hand, whilst considering the skewness, events with skewness ≥ 0 are grouped in the same category as flip +1 and vice versa (this is based on how the direction and skewness are defined and related in HAP).

By comparing the image amplitude versus BFF curves of the skewness and flip neural network, it is found that the flip network, trained on FO simulations, for direction reconstruction leads to $\sim$20% more events being correctly classified, as shown in Figure 4.5.

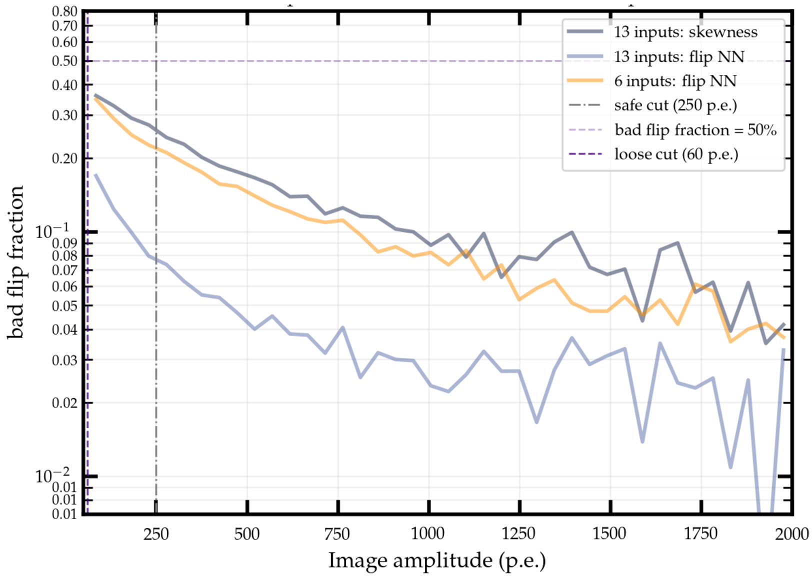

FIGURE 4.5: A comparison of the BFF for skewness-based and the flip-neural-network-based direction reconstruction. Two cases are considered: (i) a flip neural network with 13 input parameters and (blue curve), and (ii) a flip neural network with 6 input parameters. Both are tested on loose events. The flip network behaves better in both cases.

The figure also shows the performance when only 6 input parameters including no new image parameters, are used (orange) instead of the final 13 being employed now. Note how the relative gain is < 10% for the former, thereby showcasing the need for the new image parameters (Table 4.1). There are no events with amplitude $<$ 60p.e. because of the applied loose cuts. It is inevitable for the performance to worsen at very low image amplitudes (low energies, that is) because only a handful of pixels are triggered – the BFF increases for lower image amplitudes.

For higher offset angles, the offsetting of events only along one direction during simulating leads to a number inequality between the +1 and -1 events available for training (majority of events have flip -1, for example). The ideal way about this caveat would be to utilise diffuse simulations for training. This aspect is highlighted in Section 4.2.3. Note that CT5's FoV is 3.2° and for all practical purposes, considering the performance on events with relatively lower offsets works well.

Implementation in HAP

As discussed in Chapter 2, HAP currently employs the energy-disp neural networks and the skewness (computed during Hillas parametrisation) for event reconstruction. Once a preliminary evaluation of the improvements has been carried out (through the bias and BFF measures), the flip network is incorporated into the pipeline (to be used in place of the skewness). Note that HAP is also modified to include the energy and disp networks trained on the new simulations.

Following this implementation, broader evaluations of performance on the larger simulation set (through θ^2 distributions) and actual H.E.S.S. observations (through the IRFs and significance values) are carried out. The latter part is discussed in the following chapter.

θ^2 distributions

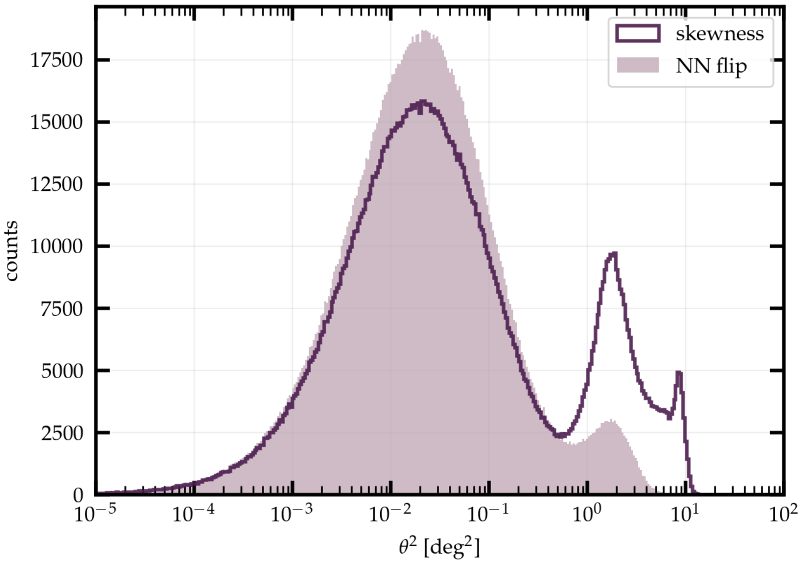

FIGURE 4.6: θ^2 distribution showcasing the improvements to the angular reconstruction method brought about by using a neural network to predict the direction. Note the reduction of the peak on the right, arising from events whose directions have been wrongly determined, when the flip network is used. The plot is for the particular case of zenith = 20°, azimuth = 180° and offset = 0.5°.

θ^2 distributions are obtained by running HAP on the larger test dataset of simulations (from which the preliminary test set was drawn) and help illustrate the degeneracy in the direction reconstruction. Figure 4.6 shows the improvements brought about by implementing the flip neural network, complementing and confirming what was demonstrated previously on a smaller test set. For consistency, the test set has equal events for both the skewness and flip network evaluations. There are two notable peaks in the histograms.

The first, larger peak on the left represents all the correctly flipped events – uncertainties in the disp calculation leads to a broadening. The position of this peak also reflects the angular resolution achieved for events whose directions were predicted correctly.

The second, smaller peak on the right, on the other hand, arises from the wrongly-flipped events. Recall how predicting the wrong side (of the ellipse) leads to a reconstructed position relatively far from the true position (a large θ). As seen in Figure 4.6, this peak is considerably diminished when the flip network is utilised.

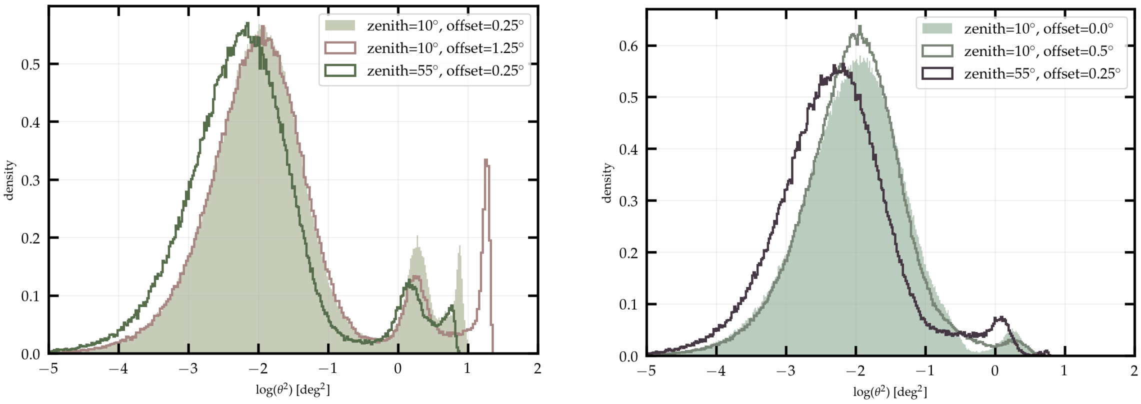

(A) reconstruction with skewness

(B) reconstruction with flip

FIGURE 4.7: θ^2 distributions showcasing the differences in reconstruction for different zeniths and offsets (the azimuth is fixed at 180°), for reconstruction using (A) the skewness and (B) the flip neural network.

Furthermore, θ^2 distributions also allow the checking for inconsistencies arising from simulations. This is demonstrated in Figure 4.7, which shows how events with different zeniths and offsets fare during angular reconstruction. It is seen that for both cases of using the skewness (Figure 4.7a) and the flip network (Figure 4.7b), the distributions follow expected behaviour:

- Events at larger zenith angles tend to be larger and possess more distinguishable skewness values as compared to showers from directly overhead (smaller zenith), which tend to be more elongated along the shower axis. This can be seen in a diminishing of the second peak, prominent in Figure 4.7a). Additionally, the energy threshold also increases with zenith which translates to a greater fraction of high-energy events, which can, in turn, be better reconstructed. This is seen as the shift of the distributions to the left for both cases.

- For a given zenith and azimuth angle, the direction reconstruction is expected to perform worse for increasing offsets because of truncation effects: it is challenging to determine the direction from incomplete images. This is indeed found to be the case as the second peak broadens (Figure 4.7a; not prominent for the flip reconstruction).

4.2.3 Training and testing on diffuse simulations

As noted in Section 4.2.2 , FO simulations do not fully capture the variability of event directions – for EAS generated from a source at a larger offset, say 1.5° (which is the edge of the CT5 FoV), only those showers lying towards the camera centre result in images. This leads to a gradual shift towards a certain flip value with increasing offset.

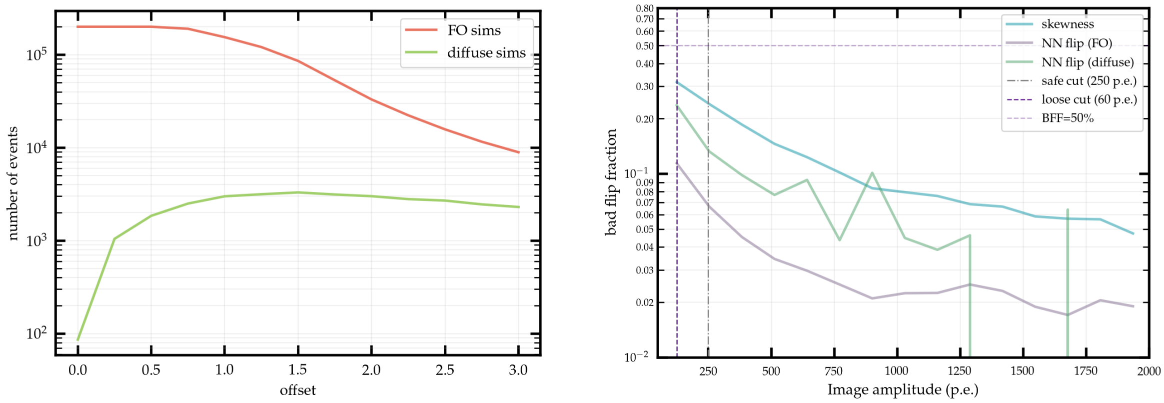

(A) Events per offset band

(B) BFF for diffuse and FO

FIGURE 4.8: A comparison between the diffuse and FO simulations as seen through (A) the number of events in each offset band and (B) the BFF fraction curves for events at zenith = 20° and azimuth = 180°. Diffuse events are selected from the [0.4°-0.6°] offset band corresponding to FO events for an offset = 0.5°.

Diffuse simulations serve as a plausible solution to this problem as events in a chosen offset band would have flip values evenly distributed between the two flip classes. However, the number of events in each offset band is limited due to computational constraints on the number of events generated. The total number of diffuse events for a given zenith and azimuth (spread across offsets in the range 0-14°), for instance, is comparable to the number of events for a given zenith, azimuth *and* offset. This discrepancy can be seen in Figure 4.8a: the number of diffuse events in a certain offset band is just not enough for the viable training of a neural network.

For instance, the number of diffuse events with an offset of 0.5 is only around 2000, as compared to 200,000 for FO events.

A comparison of the BFF between the FO and diffuse simulations was carried out and is seen in Figure 4.8b. Note how lesser events in each offset band leads to a worse performance (not enough events to train on) and larger fluctuations (not enough events per amplitude bin). The BFF curve for the diffuse simulations is obtained after weighting with respect to the FO simulations (Figure 4.8a) for consistency.

At present, ways of improving this offset dependence of the flip are being developed. One method, for example, involves the rotation and translation of images to other camera quadrants and consistently computing the corresponding change in the directional information they hold.

Chapter 5

Application to VHE γ-ray AGN

To benchmark the current mono event reconstruction techniques employed in H.E.S.S. and further quantify the improvements made to the reconstruction method, a high-level (Gammapy) analysis of a VHE gamma-ray AGN is carried out. In this chapter, the methods utilized to obtain the final science products such as fluxes and significance maps, as well as the results of the analysis are described.

5.1 Methods

5.1.1 Background estimation

During γ-hadron separation (Section 1.3.2), some hadronic events are erroneously classified as γ-ray events because of imperfect event selection. This background of fake γ-like images needs to be correctly characterized while estimating the flux from γ-ray sources.

Generally, each H.E.S.S. observation of a source is carried out in the so-called "wobble" mode – the source is alternately offset from the telescope pointing position by a small angle during the observation run (recall FO simulations in Section 3.2). Thus, the source is never present at the center of the telescope's FoV, and the side not containing the source can be used as a background control.

For a sky-map of a given observation, a test region around the source called the *ON region*, with $\mathrm{N_{on}}$ event counts, can be defined. Similarly, if $\mathrm{N_{off}}$ represents the counts in a background control region (can vary depending on the type of background estimation methods used), the γ-ray excess $\mathrm{N_{excess}}$ is given by

$$N_{excess} = N_{on} - \alpha N_{off}, \tag{5.1}$$

where α is a normalization factor which accounts for differences in angular extents, exposure-times and acceptance between the signal and background regions. The *acceptance* here is the probability of accepting a background event as γ-like. It is present in the form of a *background model* created using archival observations with regions of known γ-ray sources removed [49]. A background model is sometimes also called an *acceptance model*.

Each observation is, therefore, associated with a background model, which Gammapy utilizes while computing the excess. There is generally a 1D radial variation assumed but this may be more complicated. Although a background model provides the average background rate at the observation position, run-to-run variations need to be considered. Two commonly employed background estimation methods (visualised in Figure 5.1) are:

- **Reflected background method**: Several OFF regions, each the same size as that of the ON region, are equally offset to the pointing position. Regions near the ON region are not included to avoid contamination due to the source. Since the camera response is assumed to be radially symmetric, a background model is not needed. However, this also makes this method susceptible to any radial variations in the acceptance.

- **Ring background method**: N_{off} is obtained from a ring around the source position. Since the ring is not centered around the central pointing position the acceptance can not be constant throughout the ring and has to be accounted for while calculating α. Therefore, a model is needed for the background estimation using this method.

A discussion of various background estimation techniques employed in VHE γ-ray astrophysics can be found in [49].

5.1.2 Significance of an observation

Following background subtraction, the significance of the excess counts is determined by a *Poisson likelihood method* introduced by Li and Ma [50]. From the excess estimation, creation of *sky maps* with the excess and significance at different sky coordinate locations can be obtained. This is done by comparing the measured event and estimated background counts (computed using methods described in the previous section) in pixels grouped together within a given *correlation radius.*

A *significance distribution* can also be derived from the significance map and offers insights into the systematic uncertainties in the background estimation. For a region with no γ-ray source, provided the background model is correct, the significance distribution should be a Gaussian centred at 0 with width 1.

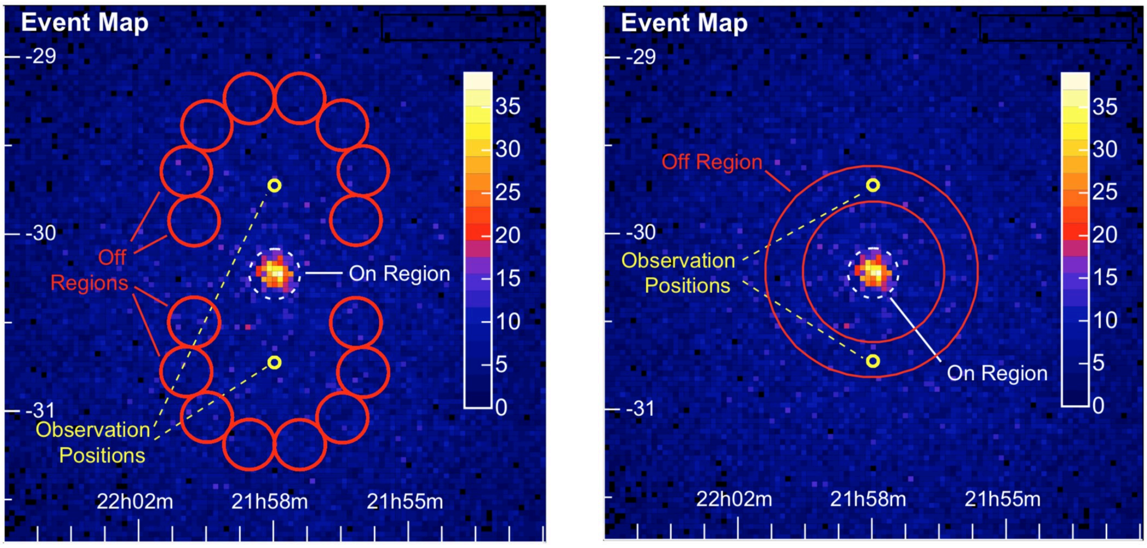

(A) Reflected-region background

(B) Ring background

FIGURE 5.1: A schematic representation of (A) the reflected-region, and (B) the ring background estimation techniques on count maps of γ-like events from a H.E.S.S. observation. For the reflected-region method, note how the OFF-regions are equally offset from the observation position, allowing for the radial variation of the camera acceptance to be intrinsically taken into account while estimating the background. Picture credit: [49].

Furthermore, θ^2 distributions (θ is the angular separation of the reconstructed direction from the source position) offer useful insights into reconstructed shower directions.

5.1.3 1D Spectral Analysis

Once the excess estimation is available, it can be used to (i) fit spectral models and (ii) obtain flux points. For the former, a spectral model (such as power law or log parabola; refer to [51]) is assumed and its prediction, after convolution with the detector/telescope response, is compared to the excess events per energy bin. The set of best-fit model parameters are determined using a maximum-likelihood approach.

The fit statistic, also referred to as the *test statistic* (TS), quantifies the goodness of fit and is given by $-2logL$, where L is the likelihood function. Depending on whether the background has been derived solely from OFF mesaurements or involves a background model, different versions of TS are used. These are detailed in [52]. For two spectral models that differ from one another by one degree of freedom, the significance of the preference for the more complex model is given by $\sqrt{\Delta TS}$, where ΔTS is the difference in the total statistics of the two model fits. Note that the prediction of the excess counts is computed using the model of interest and the IRFs, and is therefore independent of any likelihood formulation.

For flux point estimation, given a set of energy bins (not necessarily the same ones used for model-fitting), the prediction of the spectral model is normalised using the actual bin counts. Note that the source morphology is ignored [4, 53, 54, 17].

5.1.4 EBL-absorbed spectra

As discussed in Chapter 1 (Section 1.4.3), the EBL can leave an imprint on the intrinsic spectrum of a source, which is seen through a spectral softening at higher energies. The EBL-absorbed spectrum is just the EBL absorption factor (defined by a particular model of choice, say Franceschini, 2017 [55]; Section 1.4.3) multiplied with the intrinsic source spectrum such as a power law [40]. For example, the EBL absorbed spectrum assuming the intrinsic source spectrum is a power law, is given as

$$\phi(E) = e^{-\alpha\tau(E,z)} \times \phi_0(E).(\frac{E}{E_0})^{-\Gamma} \tag{5.2}$$

Here, the first term is the EBL absorption factor described in Section 1.4.3 and the second term is the power law spectral model (Γ is the spectral index).

The spectral fitting and flux point estimation is done in the same manner as discussed in the previous section. Note that along with the energy (already defined in the form of bins) the redshift of the source is also an input parameter to the model.

5.2 Application to a VHE AGN: PKS 0903-57

H.E.S.S. observations of the blazar PKS 0903-57 were carried out soon after it was reported to be in flaring state by AGILE [56] and the Fermi-LAT [57] in April 2020 [58]. The source is a BL Lac object, positioned at Right Ascension=136.222° and Declination=-57.5849° [59, 60]. A tentative redshift of 0.695 is reported in literature [61] and has been assumed in studies carried out on this blazar. However, owing to an ambiguity in its location and the presence of other sources very close by (within $4''$ and thus not resolvable by H.E.S.S.), the redshift of PKS 0903-57 needs to be confirmed [59, 62].

Long-term variability studies at high energies with Fermi and broad-band studies of the 2020 flare have been carried out [63, 64]. However, a spectral and temporal study at very high energy γ energies, which is absent for the source, is necessary to understand the underlying causes of the particle acceleration, radiation and flares taking place in these objects.

In this section, an overview of the science products from the PKS 0903-57 H.E.S.S. observations, obtained before and after improvements to the mono event reconstruction is provided. All analyses reported here have been carried out on data (and reconstruction neural networks trained) with safe cuts. Note that in addition to event reconstruction, an improvement in GHS for mono, independent of this project, was also carried out and has been included in the new analysis configuration [65].

5.2.1 IRFs

As discussed in Section 1.3.3, improvements to the low-level analysis, event reconstruction in this case, will be reflected in the IRFs of H.E.S.S. observations. The IRFs shown here are averaged over the observations (with different pointing, zenith and exposure times) considered for this analysis. In particular, the energy and angular reconstruction improvements can be visualised through the energy dispersion matrix and point spread function, respectively.

Energy dispersion

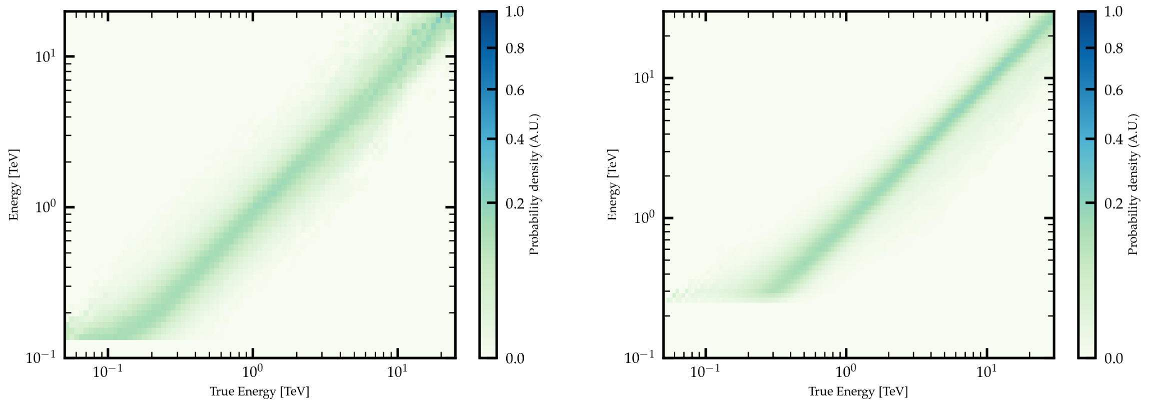

(A) Before improvements

(B) After improvements

FIGURE 5.2: Energy dispersion matrices illustrating the energy reconstruction (A) before and (B) after improvements have been carried out to the event reconstruction. Note how after improvements, for a given E_{true}, the distribution of the reconstructed energies is narrower, thereby providing a much better energy resolution.

The energy dispersion matrix quantifies the accuracy of the energy reconstruction and showcases the probability of reconstructing a γ-ray with energy E_{true} with an energy E_{reco}. The two energy dispersion matrices corresponding to the analyses carried out before and after the event reconstruction improvements are shown in Figure 5.2: the energy is predicted much better for the analysis carried out after the improvements have been implemented in the analysis pipeline. Note that the energy thresholds for the two cases are different due to intrinsic differences in the exposures which result from slightly different low-level analysis configurations (discussed further in Section 5.2.1).

Point Spread Function

The direction reconstruction accuracy is represented by the *point spread function* (PSF), which is best visualised using the *containment radius*– the angular distance within which a certain fraction, say 68% or 95%, of the signal from a point source, is contained.

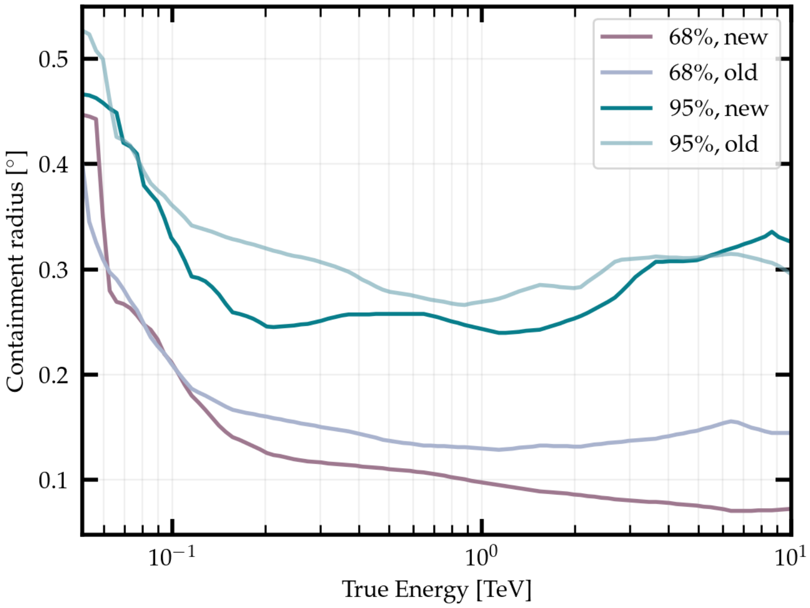

FIGURE 5.3: The containment radius as a function of energy before (old) and after (new) angular reconstruction improvement implementation. Both the 68% and 95% containment cases are shown. The containments for the new analysis are much improved in the energy range of interest for mono.

The improvements on the angular reconstruction are visualised through the energy versus containment radius curves in Figure 5.3. The figure clearly shows the significant performance improvements of upto 20% achieved with the new analysis configuration, in the energy range of interest for mono. Note that, better the angular reconstruction, smaller is the value of the containment radius.

Effective area and Exposure

The *effective collecting area* of the detector (CT5 in this case), referred to as the *effective area* or A_{eff}, depends on the offset from pointing, photon energies, the telescope's efficiency and pointing zenith. It has units of length^2. The *effective exposure*, or simply exposure, includes the energy-independent observation time with A_{eff} and has units of length^2 × time. It can therefore be used to calculate the expected number of γ-ray events from a source, whose flux (photons/m^2/s) is known. Figure 5.4 shows the exposure as a function of the energy for the analysis carried out on PKS 0903 before (old) and after (new) angular reconstruction improvements.

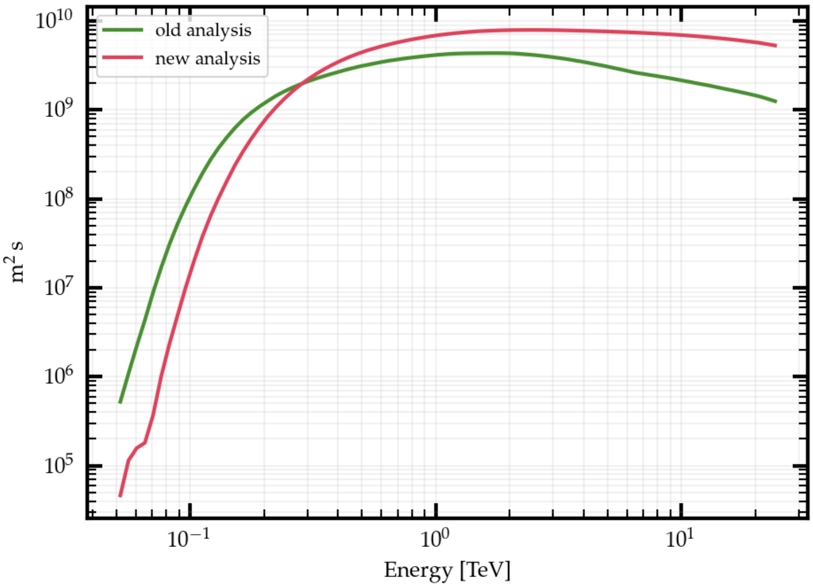

FIGURE 5.4: The exposure as a function of energy before (old) and after (new) improvements. Differences in the low-level analysis lead to the differences between the two cases.

Here, it is important to note that a completely fair and ideal comparison of detection significances, θ^2 distributions and spectral fits can be carried out only if the events selected for high-level analysis are the same. This selection includes selections carried out both at lower levels (through GHS and image cleaning) and using Gammapy. The latter involves the creation of a *safe mask* (which selects for a safe data range) based on the effective area, energy dispersion and offset limits, and leads to differences in the energy thresholds. Nonetheless, both selections play a role in comparison between the old and new analysis.

Therefore, variations in the two exposures arise because of differences in the old and new analysis configurations. Firstly, the method used for image cleaning (tailcuts versus timecleaned, respectively) and GHS cuts is different for each. Secondly, the different IRFs result in different Gammapy safe masks. Note that the observation time considered (in terms of the chosen observation runs) is the same for both analyses.

5.2.2 High-level Gammapy analysis

The H.E.S.S. observations of PKS 0903-57 taken during its flare in 2020 have been independently processed as part of the H.E.S.S. AGN task group's PKS0903-57 ToO campaign [58]. These analysis results, obtained through a complete HAP analysis, are available on the internal H.E.S.S. Confluence pages and serve as the reference for this work [66]. For consistency checks, detection significances and spectral fits obtained with the Gammapy analysis carried out for this work are compared to the results of the former.

PKS 0903-57 was observed for a total 13 hours 53 minutes by H.E.S.S. across a total of 31 runs, three of which are removed during the analysis owing to problems with bad trigger and atmosphere; 28 runs adding to a total of 13 hours and 5 minutes are finally selected. The average zenith and pointing offset for the observations are 30° and 0.5°, respectively. These lead to an initial significance of 70.55σ using the standard analysis configuration in HAP [66].

Note that, henceforth, "new" and "old" will refer to the analysis configurations with and without the event reconstruction improvements.

Significance and θ^2 distributions

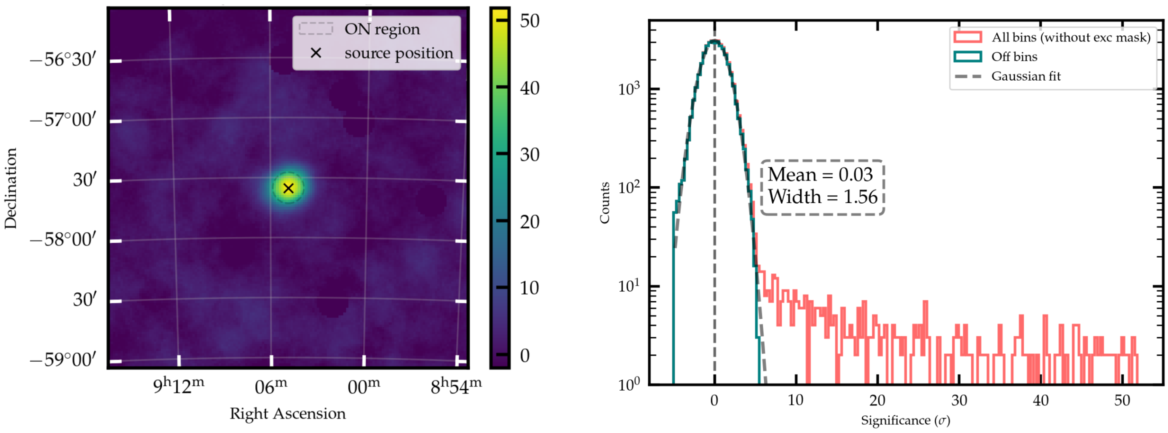

(A) Significance map (B) Significance distribution

FIGURE 5.5: The significance map in sky coordinates (A) and significance distribution (B) for the new analysis of the 2020 H.E.S.S. observations of PKS 0903-57. There is a $> 50\sigma$ excess at the position of the source. The significance distribution on the right also shows a Gaussian fit to the OFF region signal. Here, the distribution of the OFF bins is derived after masking the region around the source; a radius of 0.4° is chosen for the exclusion mask region.

The source is detected with a significance $> 50\sigma$ for both the new and old analyses. The significance map and the corresponding significance distribution obtained using the new analysis are shown in Figure 5.5. A correlation radius of 0.13° was chosen for creating the significance map.

Here, the Gaussian fit to the OFF counts data is centred around 0 (as expected) but does not have a mean of 1. This arises because of the imperfections in the background modelling and has nothing to do with the event selection or reconstruction procedures.

Figure 5.6 shows the θ^2 distributions of the significances, for both the new and old analyses. Note that the background is over-estimated for the new analysis and is not perfect (negative excess) and needs to be addressed in order to get a comparable θ^2 distribution. In addition, the event counts are also not the same for the two cases owing to differences in exposure as discussed in Section 5.2.1. These two factors – imperfect background modelling and intrinsic differences in the two analysis configurations – lead to a visible difference in the significance distribution (Figure 5.6c)

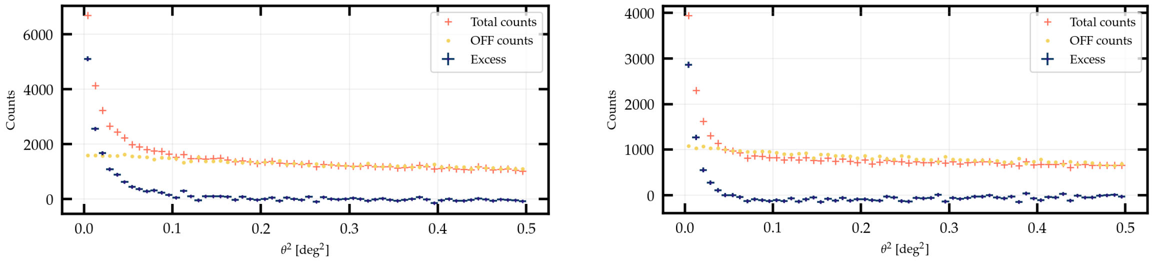

(A) Old analysis

(B) New analysis

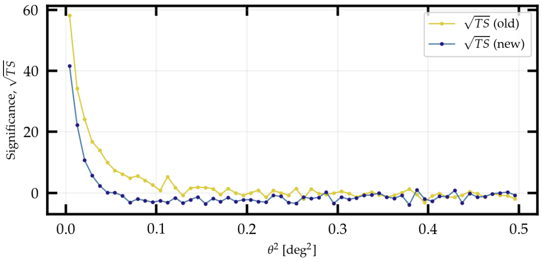

(C) significance as a function of θ^2

FIGURE 5.6: The θ^2 distributions of the counts for the new (A) and old (B) analysis. The significance as a function of θ^2 is also shown for the two cases (C).

An important point to note here is the improved angular resolution obtained for the new analysis – the θ^2 distribution is much narrower compared to the old analysis as seen for $0 \leq \theta^2 \leq 0.1$ in Figure 5.6c.

Spectral fitting and flux estimation

In order to make sure that the results of the reference HAP analysis (from the H.E.S.S. AGN group) and the Gammapy analysis in this work are consistent, the power law

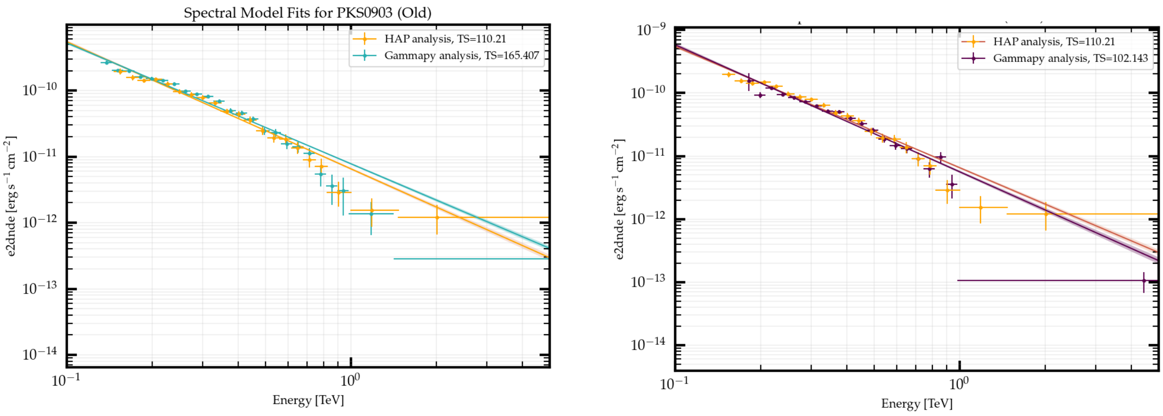

(A) old analysis (B) new analysis

FIGURE 5.7: Power law fits to the flux points derived from H.E.S.S. observations of PKS 0903-57 during its flaring state, as seen for the (A) old and (B) new analysis. As a consistency check, each is also compared to the fits obtained by a complete HAP analysis carried out by the H.E.S.S. AGN group (orange line and datapoints).

spectral model fit using Gammapy is compared to the HAP one, for both cases of the new and old analysis configurations. Since this is a 1D spectral analysis, no sky maps are created and the reflected region method is employed for background estimation; no background models are necessary.

Figure 5.7 shows the flux points and power law fits for the Gammapy and HAP analyses. Both the new and old analyses are consistent with HAP; the best-fit power law spectral indices are 4.02 ± 0.05, 3.83 ± 0.03 and 3.92 ± 0.04, respectively. The slight differences arise because of different energy thresholds for the three analyses, which, in turn, arise from the different analysis configurations and exposures.

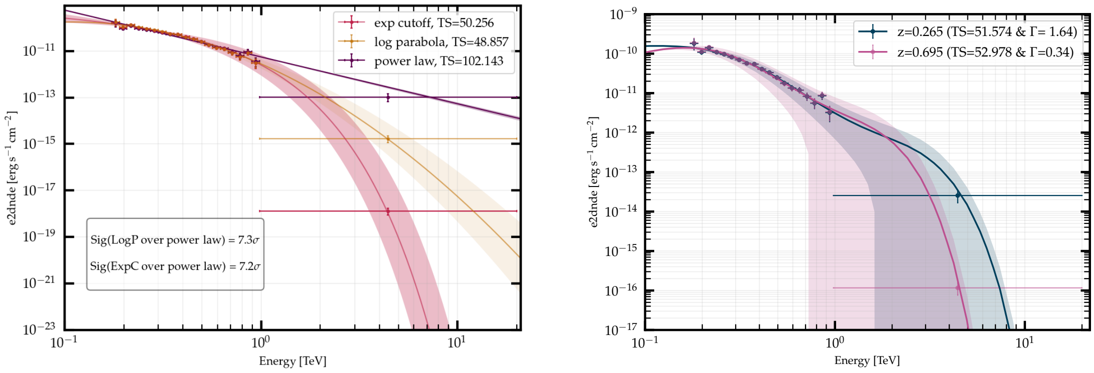

(A) old analysis (B) new analysis

FIGURE 5.8: Different spectral model (A) and EBL absorbed power law (B) fits to the flux points derived from the H.E.S.S. observations of PKS 0903-57 during its flaring state. For the absorbed power law, fits have been carried out for redshifts 0.265 and 0.695.

Figure 5.8a shows the results of fitting other spectral models, such as the log parabola and exponential cutoff to the data using the new analysis configuration. The exponential cutoff and log parabola models are preferred significantly over the power law (Figure 5.8a).

EBL-Absorbed Spectra

A mentioned previously, the redshift of PKS 0903-57 has not been precisely determined, with plausible values being 0.695 [61] and 0.265 [66]. An EBL-absorbed power law fit was carried out, assuming each of the two redshifts separately and the Franceschini (2017) EBL model [55]. The resultant spectra, obtained with the new analysis configuration, are showcased in Figure 5.8b.

The best-fit spectral indices for the redshifts 0.265 and 0.695 are 1.64 ± 0.39 and 0.34 ± 0.58, respectively. A very hard and highly improbable spectral index value for $z = 0.695$ is obtained from the fit [67]. However, without flux points at lower (from Fermi-LAT, for instance) and higher energies (with a sterero configuration in H.E.S.S.) to constrain the spectrum, it is not possible to statistically rule out either redshift.

Chapter 6

Conclusions and future work

In this chapter, a summary of the work carried out for this thesis and the conclusions that can be drawn from the results are presented. A brief discussion on plausible directions for future work is also provided.

6.1 Summary

- The need for a more robust and inclusive data analysis scheme which accesses the whole energy range of H.E.S.S. (event classes) requires a good knowledge of event reconstruction. CT5 — the central, largest telescope in the H.E.S.S. array — has the lowest energy threshold of the experiment because of its large size and camera. Its data, therefore, form an integral part of the analysis chain.
- The unavailability of a stereoscopic view for monoscopic events, however, limits the reconstruction capabilities of CT5. Currently, event reconstruction for CT5 data is two-fold: (i) the energy and disp are computed using a neural network trained on MC air shower simulations and (ii) the direction of the primary γ-ray is obtained with the skewness of the shower image.
- A set of new image parameters are utilised to train a neural network to determine the side of the ellipse's major axis on which the source lies. These variables take into account the charge and timing information encoded in a shower image as well as subtle asymmetries in the Hillas ellipse. New air shower simulations that take atmospheric variations better into account, are utilised for training and testing of the neural networks.
- The utilisation of the new image parameters and neural networks leads to significant improvements in monoscopic energy and angular reconstruction.

These can be seen through the energy and disp bias and resolution curves as well as the θ^2 distributions (Chapter 4).

- The improvements, after integration into the low-level analysis pipeline (HAP), can be showcased through the IRFs associated with real H.E.S.S. observations. This is illustrated through the average energy dispersion and point spread functions for the 2020 H.E.S.S. observations of the flaring PKS 0903-57.
- The significance and θ^2 distributions obtained for the PKS 0903-57 observations are limited by imperfect background modelling. Yet, a narrow θ^2 significance distributions shows the improvements to the monoscopic angular reconstruction.
- Differences in the low-level analysis configurations (due to event cleaning and GHS) as well as high-level selection of events (safe data range utilised by Gammapy) leads to intrinsic variations in the computed γ-ray excess, significances and energy thresholds between the old and new analysis. In particular, this is visualised by the different exposures for the old and new analyses (Section 5.2.1).
- The log parabola and exponential cutoff spectral models are found to be highly preferred over the power-law fit to the observational data of PKS 0903-57.
- A precise determination of the redshift and EBL-absorbed model is not possible with just CT5 data although an interpretational preference for the lower redshift is concluded.

6.2 Future work

- The improvements carried out on monoscopic reconstruction can now be implemented in the larger scheme of Class M in data analysis using event classes Section 2.3.1.
- Currently, image parameters based on continuous distributions of the charge and timing information contained in air shower images are being tested and implemented in GHS for CT5. With the monoscopic improvements brought about by utilising the new image parameters, the implementation of a more intuitive and natural approach with continuous variables for angular reconstruction seems apt and has been planned as the next step for the event class analysis chain.

- As discussed in Section 4.2.3, diffuse simulations serve as ideal datasets on which to train and test changes to data analysis. However, their production is limited by computational constraints. A way around this could be to utilise air showers simulated in a ring around the camera centre or with the source mirrored on either side of the camera axis as opposed to FO simulations (offset to only one side) utilised at present. This would also allow for the quadrant dependency of the flip value and number inequality between +1 and -1 events at higher offsets (Section 4.2.2), to be reduced.

- In Section 5.2.2, a discrepancy in the significance distribution for the new analysis — width $\neq 1$ in Figure 5.5b and count overestimation in Figure 5.6b — was showcased. Corrections to the imperfect background modelling responsible for this is the next step forward in getting more comparable analysis results. Furthermore, a Gammapy analysis of the PKS 0903-57 observations events selected with an ultra loose analysis configuration (Section 4.1.2) and correct background modelling would be a natural progression towards characterising the performance of the improved monoscopic reconstruction techniques on low-energy events.

- As reported in Section 5.2.2, the disagreement between the EBL-absorbed power law model indices for the redshifts 0.265 and 0.695 do not necessarily imply the preference for the former. An actual comparison can be made only after the consideration of data at lower energies, such as that from Fermi-LAT [57]. In fact, such an analysis is already being carried out by the PKS0903 ToO campaign [66]. Additionally, the redshift itself can be set as a free parameter.

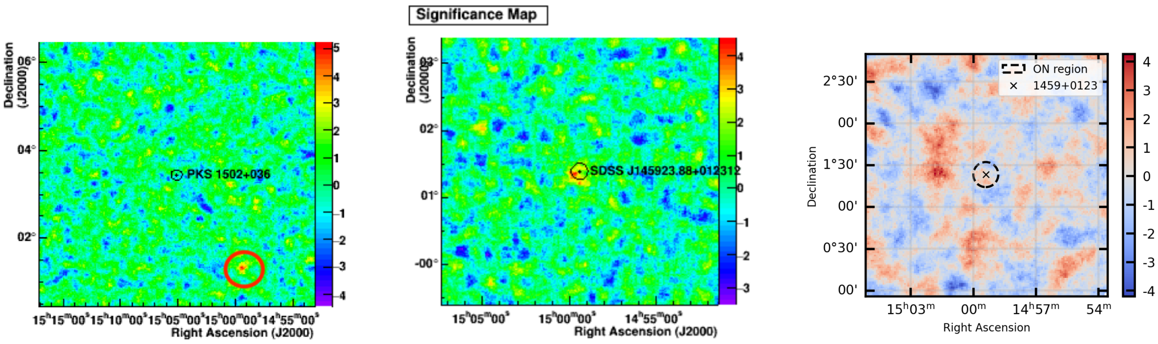

(A) Model++ (2022) (B) Model++ (2023) (C) HAP-Gammapy (2023)

FIGURE 6.1: The Model++ analysis of the H.E.S.S. observations of (A) PKS1502+036 that reveals a hotspot at the position of J145923.9+012312 in 2022, and (B) J145923.9+012312 that once again shows an excess at the source position (2023 data). Finally, the HAP and Gammapy analysis of the 2023 H.E.S.S. data for J145923.9+012312 (C) shows no excess.

- In 2022, an independent, stereo analysis by Model++ (another H.E.S.S. data analysis pipeline like HAP) of the H.E.S.S. observations for PKS1502+036 revealed a γ-ray hotspot at the position of the quasar J145923.9+012312 (Figure 6.1a) [68, 69]. To confirm a detection at this position, a HAP and Gammapy analysis using the old, safe mono configuration was carried out on this observational data. J145923.9+012312 was, however, found to be out of the mono FoV for an offset cut of 1.6 deg.

  In 2023, observations centred at the putative source J145923.9+012312 were taken [68, 69]. Although a stereo Model++ analysis once again found an excess at the source position (Figure 6.1b), a HAP and Gammapy safe mono analysis showed no detection (Figure 6.1c). The next step, therefore, would be to carry out a further analysis of this source with the new, improved safe as well as the ultra loose configurations.

Bibliography

[1] Bing Zhang and Peter Mészáros. "Preface: High energy astrophysics". In: *Frontiers of Physics* 8.6 (Dec. 2013), pp. 605–608. DOI: `10.1007/s11467-013-0351-7`. arXiv: `1401.6613 [astro-ph.HE]`.

[2] A. De Angelis and M. Mallamaci. "Gamma-ray astrophysics". In: *European Physical Journal Plus* 133.8, 324 (Aug. 2018), p. 324. DOI: `10.1140/epjp/i2018-12181-0`. arXiv: `1805.05642 [astro-ph.HE]`.

[3] Wei Cui. "TeV gamma-ray astronomy". In: *Research in Astronomy and Astrophysics* 9.8 (Aug. 2009), pp. 841–860. DOI: `10.1088/1674-4527/9/8/001`. arXiv: `0907.4052 [astro-ph.HE]`.

[4] F. Acero et al. "Fermi Large Area Telescope Third Source Catalog". In: *The Astrophysical Journal Supplement Series* 218.2, 23 (June 2015), p. 23. DOI: `10.1088/0067-0049/218/2/23`. arXiv: `1501.02003 [astro-ph.HE]`.

[5] D. Bose et al. "Ground-based gamma-ray astronomy: history and development of techniques". In: *European Physical Journal Special Topics* 231.1 (Jan. 2022), pp. 3–26. DOI: `10.1140/epjs/s11734-021-00396-3`. arXiv: `2201.04719 [astro-ph.IM]`.

[6] Mathieu de Naurois and Daniel Mazin. "Ground-based detectors in very-high-energy gamma-ray astronomy". In: *Comptes Rendus Physique* 16.6-7 (Aug. 2015), pp. 610–627. DOI: `10.1016/j.crhy.2015.08.011`. arXiv: `1511.00463 [astro-ph.IM]`.

[7] F. Aharonian et al. "High energy astrophysics with ground-based gamma ray detectors". In: *Reports on Progress in Physics* 71.9, 096901 (Sept. 2008), p. 096901. DOI: `10.1088/0034-4885/71/9/096901`.

[8] D. Heck et al. *CORSIKA: a Monte Carlo code to simulate extensive air showers.* 1998. URL: `https://www.iap.kit.edu/corsika/index.php`.

[9] Thomas K Gaisser, Ralph Engel, and Elisa Resconi. *Cosmic rays and particle physics*. Cambridge University Press, 2016.

[10] John David Jackson. *Classical electrodynamics*. John Wiley & Sons, 2012.

[11] Armelle Jardin-Blicq. *The TeV γ-ray emission of the Galactic Plane*. PhD thesis, University of Heidelberg. 2019. URL: `https://www.imprs-hd.mpg.de/398523/thesis_Jardin-Blicq.pdf`.

[12] A. M. Hillas. "Evolution of ground-based gamma-ray astronomy from the early days to the Cherenkov Telescope Arrays". In: *Astroparticle Physics* 43 (Mar. 2013), pp. 19–43. DOI: `10.1016/j.astropartphys.2012.06.002`.

[13] The H.E.S.S. Collboration. *H.E.S.S. (the High Energy Stereoscopic System)*. 2021. URL: `https://www.mpi-hd.mpg.de/HESS/`.

[14] eoPortal. *HESS (High Energy Stereoscopic System)*. Observation of the Earth and its Environment: other space activities. 2020. URL: `https://www.eoportal.org/other-space-activities/hess#hess-telescopes`.

[15] H. E. S. S. Collaboration et al. "Gamma-ray blazar spectra with H.E.S.S. II mono analysis: The case of <ASTROBJ>PKS 2155-304</ASTROBJ> and <ASTROBJ>PG 1553+113</ASTROBJ>". In: *Astronomy and Astrophysics* 600, A89 (Apr. 2017), A89. DOI: `10.1051/0004-6361/201629427`. arXiv: `1612.01843 [astro-ph.HE]`.

[16] Gerd Pühlhofer. "H.E.S.S. highlights". In: *arXiv e-prints*, arXiv:1801.06074 (Jan. 2018), arXiv:1801.06074. DOI: `10.48550/arXiv.1801.06074`. arXiv: `1801.06074 [astro-ph.HE]`.

[17] Cosimo Nigro, Tarek Hassan, and Laura Olivera-Nieto. "Evolution of Data Formats in Very-High-Energy Gamma-Ray Astronomy". In: *Universe* 7.10, 374 (Oct. 2021), p. 374. DOI: `10.3390/universe7100374`. arXiv: `2109.14661 [astro-ph.IM]`.

[18] Konrad Bernlöhr. "Simulation of imaging atmospheric Cherenkov telescopes with CORSIKA and sim_ telarray". In: *Astroparticle Physics* 30.3 (Oct. 2008), pp. 149–158. DOI: `10.1016/j.astropartphys.2008.07.009`. arXiv: `0808.2253 [astro-ph]`.

[19] F. Aharonian et al. "Observations of the Crab nebula with HESS". In: *Astronomy and Astrophysics* 457.3 (Oct. 2006), pp. 899–915. DOI: `10.1051/0004-6361:20065351`. arXiv: `astro-ph/0607333 [astro-ph]`.

[20] Denys Malyshev and Lars Mohrmann. "Analysis Methods for Gamma-ray Astronomy". In: *Handbook of X-ray and Gamma-ray Astrophysics (eds. C. Bambi*. 2023, 137, p. 137. DOI: `10.1007/978-981-16-4544-0_177-1`.

[21] A. M. Hillas. "Cerenkov Light Images of EAS Produced by Primary Gamma Rays and by Nuclei". In: *19th International Cosmic Ray Conference (ICRC19), Volume 3*. Vol. 3. International Cosmic Ray Conference. Aug. 1985, p. 445.

[22] S. Ohm, C. van Eldik, and K. Egberts. “γ/hadron separation in very-high-energy γ-ray astronomy using a multivariate analysis method”. In: *Astroparticle Physics* 31.5 (June 2009), pp. 383–391. DOI: `10.1016/j.astropartphys.2009.04.001`. arXiv: `0904.1136 [astro-ph.IM]`.

[23] F. A. Aharonian et al. “The potential of ground based arrays of imaging atmospheric Cherenkov telescopes. I. Determination of shower parameters”. In: *Astroparticle Physics* 6.3-4 (Mar. 1997), pp. 343–368. DOI: `10.1016/S0927-6505(96)00069-2`.

[24] R. D. Parsons and J. A. Hinton. “A Monte Carlo template based analysis for air-Cherenkov arrays”. In: *Astroparticle Physics* 56 (Apr. 2014), pp. 26–34. DOI: `10.1016/j.astropartphys.2014.03.002`. arXiv: `1403.2993 [astro-ph.IM]`.

[25] Axel Donath et al. “Gammapy: A Python package for gamma-ray astronomy”. In: *A&A* 678 (2023), A157. DOI: `10.1051/0004-6361/202346488`. URL: `https://doi.org/10.1051/0004-6361/202346488`.

[26] Arnau Aguasca-Cabot et al. *Gammapy: Python toolbox for gamma-ray astronomy*. Version v1.1. June 2023. URL: `https://zenodo.org/records/8033275`.

[27] The H.E.S.S. Collboration. *Astrophysics with the High Energy Stereoscopic System)*. 2021. URL: `https://www.mpi-hd.mpg.de/HESS/pages/about/physics/`.

[28] B. V. Komberg. “Quasars and active galactic nuclei.” In: *Astrophysics on the Threshold of the 21st Century*. Ed. by N. S. Kardashev. 1992, pp. 253–276.

[29] Gregory A. Shields. “A Brief History of Active Galactic Nuclei”. In: *The Publications of the Astronomical Society of the Pacific* 111.760 (June 1999), pp. 661–678. DOI: `10.1086/316378`. arXiv: `astro-ph/9903401 [astro-ph]`.

[30] Roger Blandford, David Meier, and Anthony Readhead. “Relativistic Jets from Active Galactic Nuclei”. In: *Annual Review of Astronomy and Astrophysics* 57 (Aug. 2019), pp. 467–509. DOI: `10.1146/annurev-astro-081817-051948`. arXiv: `1812.06025 [astro-ph.HE]`.

[31] P. Padovani et al. “Active galactic nuclei: what’s in a name?” In: *The Astronomy and Astrophysics Review* 25.1, 2 (Aug. 2017), p. 2. DOI: `10.1007/s00159-017-0102-9`. arXiv: `1707.07134 [astro-ph.GA]`.

[32] Paolo Padovani. “Active Galactic Nuclei at all wavelengths and from all angles”. In: *Frontiers in Astronomy and Space Sciences* 4, 35 (Nov. 2017), p. 35. DOI: `10.3389/fspas.2017.00035`.

[33] Marie-Luise Menzel. *Narrow line kinematics in a spectroscopic survey of X-ray selected AGN in the XMM-XXL North*. PhD thesis, Ludwig–Maximilians–Universität München. 2016. URL: `https://www.imprs-astro.mpg.de/sites/default/files/menzel.pdf`.

[34] C. Megan Urry and Paolo Padovani. "Unified Schemes for Radio-Loud Active Galactic Nuclei". In: *Publications of the Astronomical Society of the Pacific* 107 (Sept. 1995), p. 803. DOI: `10.1086/133630`. arXiv: `astro-ph/9506063 [astro-ph]`.

[35] M. Punch et al. "Detection of TeV photons from the active galaxy Markarian 421". In: *Nature* 358.6386 (Aug. 1992), pp. 477–478. DOI: `10.1038/358477a0`.

[36] Maria Petropoulou, Stefan Coenders, and Stavros Dimitrakoudis. "Time-dependent neutrino emission from Mrk 421 during flares and predictions for IceCube". In: *Astroparticle Physics* 80 (July 2016), pp. 115–130. DOI: `10.1016/j.astropartphys.2016.04.001`. arXiv: `1603.06954 [astro-ph.HE]`.

[37] Asantha Cooray. "Extragalactic background light measurements and applications". In: *Royal Society Open Science* 3.3 (Mar. 2016), p. 150555. DOI: `10.1098/rsos.150555`. arXiv: `1602.03512 [astro-ph.CO]`.

[38] H.E.S.S. Collaboration. *Probing Extragalactic Background Light with 1ES 0229+200*. 2021. URL: `https://www.mpi-hd.mpg.de/HESS/pages/home/som/2007/11/`.

[39] H.E.S.S. Collaboration. *The Blazar 1ES 1101-232 and the Gamma Ray Horizon*. 2021. URL: `https://www.mpi-hd.mpg.de/HESS/pages/home/som/2005/12/`.

[40] H.E.S.S. Collaboration. *EBL absorption spectral model*. 2024. URL: `https://docs.gammapy.org/1.2/user-guide/model-gallery/spectral/plot_absorbed.html`.

[41] Fons Rademakers et al. *ROOT - An Object-Oriented Data Analysis Framework. root-project/root: v6.10/04*. Version v6-10-04. Aug. 2017. DOI: `10.5281/zenodo.848819`.

[42] A. Hoecker et al. "TMVA - Toolkit for Multivariate Data Analysis". In: *arXiv e-prints*, physics/0703039 (Mar. 2007), physics/0703039. DOI: `10.48550/arXiv.physics/0703039`. arXiv: `physics/0703039 [physics.data-an]`.

[43] Aurélien Géron. *Hands-on machine learning with Scikit-Learn, Keras, and TensorFlow*. " O'Reilly Media, Inc.", 2022.

[44] 3blue1brown. *Neural networks*. `https://www.youtube.com/playlist?",list=PLZHQObOWTQDNU6R1_67000Dx_ZCJB-3pi`. 2017.

[45] Michael A Nielsen. *Neural networks and deep learning*. Vol. 25. Determination press San Francisco, CA, USA, 2015.

[46] IBM. *What is a neural network?* 2023. URL: `https://www.ibm.com/topics/neural-networks`.

[47] Martín Abadi et al. *TensorFlow: Large-Scale Machine Learning on Heterogeneous Systems*. Software available from tensorflow.org. 2015. URL: `https://www.tensorflow.org/`.

[48] François Chollet et al. *Keras*. `https://keras.io`. 2015.

[49] D. Berge, S. Funk, and J. Hinton. "Background modelling in very-high-energy γ-ray astronomy". In: *Astronomy and Astrophysics* 466.3 (May 2007), pp. 1219–1229. DOI: `10.1051/0004-6361:20066674`. arXiv: `astro-ph/0610959 [astro-ph]`.

[50] T. -P. Li and Y. -Q. Ma. "Analysis methods for results in gamma-ray astronomy." In: *Astrophysical Journa* 272 (Sept. 1983), pp. 317–324. DOI: `10.1086/161295`.

[51] Gammapy. *The Gammapy model gallery: Spectral models*. 2024. URL: `https://docs.gammapy.org/1.2/user-guide/model-gallery/index.html`.

[52] Gammapy. *Fit statistics*. 2024. URL: `https://docs.gammapy.org/dev/user-guide/stats/fit_statistics.html#fit-statistics`.

[53] H. E. S. S. Collaboration et al. "The H.E.S.S. Galactic plane survey". In: *Astronomy & Astrophysics* 612, A1 (Apr. 2018), A1. DOI: `10.1051/0004-6361/201732098`. arXiv: `1804.02432 [astro-ph.HE]`.

[54] Data formats for gamma-ray astronomy. *Bin-by-bin Likelihood Profiles*. 2018. URL: `https://gamma-astro-data-formats.readthedocs.io/en/latest/spectra/binned_likelihoods/index.html`.

[55] Alberto Franceschini and Giulia Rodighiero. "The extragalactic background light revisited and the cosmic photon-photon opacity". In: *Astronomy and Astrophysics* 603, A34 (July 2017), A34. DOI: `10.1051/0004-6361/201629684`. arXiv: `1705.10256 [astro-ph.HE]`.

[56] F. Lucarelli et al. "AGILE detection of enhanced gamma-ray activity from the blazar PKS 0903-57". In: *The Astronomer's Telegram* 13602 (Apr. 2020), p. 1.

[57] Sara Buson. "Fermi-LAT discovery of VHE emission from blazar PKS 0903-57". In: *The Astronomer's Telegram* 13604 (Apr. 2020), p. 1.

[58] S. J. Wagner. "Detection of Very-High-Energy Gamma-rays from PKS 0903-57 by H.E.S.S." In: *The Astronomer's Telegram* 13632 (Apr. 2020), p. 1.

[59] Julien Lefaucheur and Santiago Pita. “Research and characterisation of blazar candidates among the Fermi/LAT 3FGL catalogue using multivariate classifications”. In: *Astronomy & Astrophysics* 602, A86 (June 2017), A86. DOI: `10.1051/0004-6361/201629552`. arXiv: `1703.01822 [astro-ph.HE]`.

[60] Alan L. Fey et al. “Astrometry of 25 Southern Hemisphere Radio Sources from a VLBI Short-Baseline Survey”. In: *The Astronomical Journal* 128.5 (Nov. 2004), pp. 2593–2598. DOI: `10.1086/424941`.

[61] D. J. Thompson, S. Djorgovski, and R. de Carvalho. “Spectroscopy of Radio Sources from the Parkes 2700 MHz Survey”. In: *Publications of the Astronomical Society of the Pacific* 102 (Nov. 1990), p. 1235. DOI: `10.1086/132758`.

[62] H. L. Marshall et al. “A Chandra Survey of Quasar Jets: First Results”. In: *The Astrophysical Journal Supplement Series* 156.1 (Jan. 2005), pp. 13–33. DOI: `10.1086/425578`. arXiv: `astro-ph/0409566 [astro-ph]`.

[63] Sandeep Kumar Mondal et al. “Spectral Modeling of Flares in Long-term Gamma-Ray Light Curve of PKS 0903-57”. In: *The Astrophysical Journal* 922.2, 160 (Dec. 2021), p. 160. DOI: `10.3847/1538-4357/ac11fa`. arXiv: `2107.02702 [astro-ph.HE]`.

[64] Zahir Shah et al. “Unveiling the broad-band spectral and temporal properties of PKS 0903-57 during its brightest flare”. In: *Monthly Notices of the Royal Astronomical Society* 504.1 (June 2021), pp. 416–427. DOI: `10.1093/mnras/stab834`. arXiv: `2103.13657 [astro-ph.HE]`.

[65] Prajath Bedur Ramesh. *Improving H.E.S.S. Monoscopic Gamma-Hadron Separation at Low Energies and Application to the Vela Pulsar*. Master’s thesis, IISER Tirupati. 2024.

[66] Michael Zacharias et al. *PKS 0903-57: ToO Campaign 2020*. 2020.

[67] M. Ajello et al. “The Cosmic Evolution of Fermi BL Lacertae Objects”. In: *The Astrophysical Journal* 780.1, 73 (Jan. 2014), p. 73. DOI: `10.1088/0004-637X/780/1/73`. arXiv: `1310.0006 [astro-ph.CO]`.

[68] Héctor Rueda et al. *AGN Round-Up Analysis*. Presentation at the 2023 HESS Spring Collaboration Meeting. 2023.

[69] Michael Zacharias et al. *Did we see a source at position 1459+0123?* Presentation at the 2023 HESS Spring Collaboration Meeting. 2023.